An imaging polarimetry survey of Type Ia supernovae: are peculiar extinction and polarization properties produced by circumstellar or interstellar matter?

Matthew R. Chu,[1]★ Aleksandar Cikota [ORCID],[2,3] Dietrich Baade,[4] Ferdinando Patat,[4] Alexei V. Filippenko,[5,6] J. Craig Wheeler [ORCID],[7] Justyn Maund [ORCID],[8] Mattia Bulla [ORCID],[9] Yi Yang,[5] Peter Höflich[10] and Lifan Wang[11]

[1]*Department of Physics, University of California, Berkeley, CA 94720-7300, USA*
[2]*European Organisation for Astronomical Research in the Southern Hemisphere (ESO), Alonso de Cordova 3107, Vitacura, Casilla 19001, Santiago de Chile, Chile*
[3]*E.O. Lawrence Berkeley National Laboratory, 1 Cyclotron Rd., Berkeley, CA 94720, USA*
[4]*European Organisation for Astronomical Research in the Southern Hemisphere (ESO), Karl-Schwarzschild-Str. 2, D-85748 Garching b. München, Germany*
[5]*Department of Astronomy, University of California, Berkeley, CA 94720-3411, USA*
[6]*Miller Institute for Basic Research in Science, University of California, Berkeley, CA 94720, USA*
[7]*Department of Astronomy, University of Texas, Austin, TX 78712-1205, USA*
[8]*Department of Physics and Astronomy, University of Sheffield, Hicks Building, Hounsfield Road, Sheffield S3 7RH, UK*
[9]*The Oskar Klein Centre, Department of Astronomy, Stockholm University, AlbaNova, SE-10691 Stockholm, Sweden*
[10]*Department of Physics, Florida State University, Tallahassee, FL 32306-4350, USA*
[11]*Department of Physics, Texas A&M University, College Station, TX 77843, USA*

ABSTRACT

Some highly reddened Type Ia supernovae (SNe Ia) display low total-to-selective extinction ratios ($R_V \lesssim 2$) in comparison to that of typical Milky Way dust ($R_V \approx 3.3$), and polarization curves that rise steeply to blue wavelengths, with peak polarization values at short wavelengths ($\lambda_{max} < 0.4\,\mu$m) in comparison to the typical Galactic values ($\lambda_{max} \approx 0.55\,\mu$m). Understanding the source of these properties could provide insight into the progenitor systems of SNe Ia. We aim to determine whether they are the result of the host galaxy's interstellar dust or circumstellar dust. This is accomplished by analysing the continuum polarization of 66 SNe Ia in dust-rich spiral galaxies and 13 SNe Ia in dust-poor elliptical galaxies as a function of normalized galactocentric distance. We find that there is a general trend of SNe Ia in spiral galaxies displaying increased polarization values when located closer to the host galaxies' centre, while SNe Ia in elliptical host galaxies display low polarization. Furthermore, all highly polarized SNe Ia in spiral host galaxies display polarization curves rising toward blue wavelengths, while no evidence of such polarization properties is shown in elliptical host galaxies. This indicates that the source of the peculiar polarization curves is likely the result of interstellar material as opposed to circumstellar material. The peculiar polarization and extinction properties observed toward some SNe Ia may be explained by the radiative torque disruption mechanism induced by the SN or the interstellar radiation field.

Key words: polarization – supernovae: general – ISM: general.

1 INTRODUCTION

Type Ia supernovae (SNe Ia) are used as standardizable candles on cosmological scales; as such, measuring their redshift and apparent brightness can quantify the expansion of the observable Universe (Riess et al. 1998; Perlmutter et al. 1999). To understand the evolution (if any) of their peak luminosity with redshift, it is imperative to accurately identify their progenitor systems. These SNe are explosions of carbon-oxygen white dwarfs (WDs) near the Chandrasekhar limit, but identifying their exact progenitor systems from current observational results is not yet conclusive (Maoz, Mannucci & Nelemans 2014). However, the nature of the progenitor systems may be encrypted in dust along lines of sight to SNe Ia,

since single-degenerate and double-degenerate models may imply different circumstellar environments (Livio & Mazzali 2018).

Prior works reveal that some highly-reddened SNe Ia, with $E(B - V) \gtrsim 1$ mag, display two unusual characteristics: (i) low total-to-selective extinction values of $R_V \lesssim 2$ (e.g. Nobili & Goobar 2008; Wang et al. 2009b; Folatelli et al. 2010; Burns et al. 2014; Amanullah et al. 2015) in comparison to typical Milky Way (MW) dust with $R_V = 3.32 \pm 0.18$ (Schlafly et al. 2016) or dust in the Large Magellanic Cloud with a wide range of R_V values between 3 and 6 (Urbaneja et al. 2017), and (ii) polarization curves steeply growing toward blue wavelengths and peaking at wavelengths below 0.4 μm (Patat et al. 2015; Zelaya et al. 2017), compared to typical Galactic Serkowski-like polarization curves that peak at $\sim 0.55\,\mu$m (Serkowski, Mathewson & Ford 1975). In general, low R_V values are correlated with smaller dust grains (Draine 2003). Along the sightlines toward SNe Ia, a high abundance of small dust grains may

★ E-mail: mrchu39@berkeley.edu

be a result of rotational disruption of larger dust grains by radiative torques in strong radiation fields, a phenomenon proposed by Hoang et al. (2019) and Hoang (2021). Furthermore, the wavelength of peak polarization, λ_{max}, is found to depend on the dust grains' size distribution (Serkowski et al. 1975; Draine & Fraisse 2009; Hoang, Lazarian & Martin 2013, 2014; Hoang 2017). In the case of an enhanced abundance of small grains, the peak moves toward blue wavelengths. There is also a correlation of the interstellar extinction law with the wavelength of maximum polarization. For typical dust in the Milky Way, Whittet & van Breda (1978) deduced $R_V = (5.6 \pm 0.3)\lambda_{max}$, where λ_{max} is in μm. On the other hand, the steeply rising polarization curves can also be explained by Rayleigh scattering from nearby dust, which produces polarization curves proportional to λ^{-4} (Andersson et al. 2013; Patat et al. 2015). Thus, the steeply rising polarization curves toward blue wavelengths can be explained by linear dichroism of aligned dust grains located in the interstellar medium (ISM) with a high abundance of small dust grains located, or alternatively by scattering from nearby circumstellar dust within the progenitor system.

A reason to believe that the peculiar polarization curves are a result of scattering from circumstellar material (CSM) is the similarity between polarization curves of SNe Ia and of protoplanetary nebulae (PPNe; Cikota et al. 2017). Depending on the nature of the companion of the exploding WD, several varieties might produce CSM. Asymptotic giant branch (AGB) stars, after evolving into PPNe, display polarization profiles similar to those observed toward SNe Ia (Patat et al. 2015). The curves in PPNe are shown to be produced by CSM scattering (Oppenheimer et al. 2005). Therefore, the common continuum polarization properties between PPNe and SNe Ia might be an indication that some SNe Ia explode within a PPN after the WD (formed from the initially more-massive star) merges with the core of the companion AGB star during the common-envelope phase (core-degenerate scenario; Kashi & Soker 2011; see also Jones & Boffin 2017; Soker 2019a, b; Hsiao et al. 2020; Ashall et al. 2021; Chiotellis, Boumis & Spetsieri 2021; Wu et al. 2021).

Research conducted by Bulla et al. (2018a) and Bulla, Goobar & Dhawan (2018b) suggests the contrary, that the dust responsible for the observed extinction in some SNe Ia is the result of interstellar material. Assuming a spherical dust shell and using Monte Carlo simulations, they demonstrated that the evolution of the SN light curves, particularly the colour excess $E(B - V)$, can place strong constraints on the distance between dust and the SN. Bulla et al. (2018b) find a time-variable colour excess for 15 out of their sample of 48 SNe Ia, and constrain dust distances between 0.013 pc and 45 pc. The constant colour excess inferred for the rest of the sample was consistent with dust located at distances $\gtrsim$ 0.5 pc. They also find that SNe with relatively nearby dust (<1 pc) are located close to the nuclei of their host galaxies, where (in the dusty high-density region) interaction between dust and the SN radiation is more likely. Furthermore, for SNe showing time-variable reddening, Bulla et al. (2018b) notice a possible preference for low R_V values. This may suggest that cloud–cloud collisions driven by the radiation pressure of SNe produce a high abundance of small dust grains, as proposed by Hoang (2017; see also Giang, Hoang & Tram 2020, who predict time-varying polarization, extinction, and colour of SNe Ia owing to rotational disruption of dust grains).

Phillips et al. (2013) found a correlation between the strength of the diffuse interstellar band (DIB) at 5780 Å along the sightlines to SNe Ia and extinction A_V. Because DIBs are characteristic of ISM in our Galaxy, and not of CSM, they suggest that the dust responsible for the extinction toward some SNe Ia is predominantly located in the ISM of the host galaxy. Phillips et al. (2013) also found that one
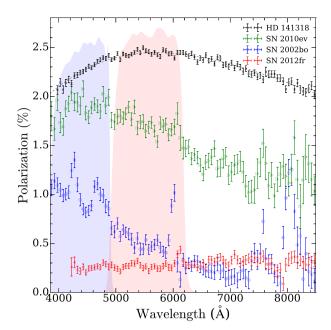

Figure 1. Examples of polarization curves observed toward SNe Ia, compared to a typical Serkowski-like polarization curve observed toward HD 141318 (Cikota et al. 2018). SN 2010ev, SN 2002bo, and SN 2012fr were observed with FORS1 or FORS2 at a phase of −1.1, −1.4, and −6.9 d relative to peak brightness, respectively (Cikota et al. 2019). Also shown are the FORS2 *B*- and *V*-band filter profiles.

quarter of their sample of 32 SNe Ia display anomalously large Na I column densities with blueshifted Na I D lines, suggesting that there is outflowing circumstellar gas around some SNe. Interestingly, not all SNe that display strong Na I D lines suffer from dust reddening, and some SNe with independent evidence of CSM do not display strong Na I D lines (Phillips et al. 2013).

This work aims to determine whether the peculiar dust properties observed toward some SNe Ia are produced by dust in the circumstellar or interstellar medium. Our main goal is to answer whether many SN Ia progenitors reside in environments with peculiar dust properties, are they surrounded by peculiar dust as a tracer of the evolution of the mass donor, or do the explosions radiatively modify nearby interstellar dust. We investigate the continuum polarization of a sample of SNe Ia and look for relations between the degree of polarization of the SN and the galactocentric distance, for different morphological galaxy types.

Polarimetry allows us to examine the dust along the line-of-sight 'in one shot,' independent of the epoch of the SN Ia, because the intrinsic continuum polarization of SNe Ia is generally negligible ($\lesssim$ 0.2 per cent; see Wang & Wheeler 2008). In addition, the line polarization is <1 per cent, so the polarized lines do not significantly contaminate continuum measurements (Fig. 1; see also examples of polarization curves in Zelaya et al. 2017, their figs 2 and 3). In contrast, to determine the reddening using photometry, multiple epochs are required to fit the light curve with intrinsic SN templates. Furthermore, from the slope of the polarization curve (derived from measurements in two different passbands), we can determine whether the polarization curve is consistent with the normal Serkowski-like curve and likely a result of linear dichroism in non-spherical grains (located in the ISM), or rising toward blue wavelengths and possibly induced by scattering from nearby clouds (dust in the CSM).

High polarization along sightlines toward SNe Ia located far away from the centres of their host galaxies, where we expect

low amounts of interstellar dust, or in elliptical galaxies, which are known to be dust poor (Smith et al. 2012; Cikota, Deustua & Marleau 2016), would provide strong evidence for polarization arising from dust within CSM and support, for example, the core-degenerate scenario (Livio & Riess 2003; Kashi & Soker 2011; Ilkov & Soker 2012, 2013). On the other hand, if we do not observe high polarization values for SNe Ia in dust-poor elliptical galaxies, and/or if there is a dependence of the steeply rising polarization curves on galactocentric distance in dust-rich spiral galaxies, this would support the hypothesis that the peculiar polarization curves are produced by host-galaxy ISM.

In Section 2 we describe the observations and the SN sample. Section 3 explains the data reduction, the interstellar polarization removal, the determination of the normalized galactocentric distances of the SNe in their host galaxies, and the morphological classification of the host galaxies. The results are presented and discussed in Section 4 and summarized in Section 5.

2 TARGETS AND OBSERVATIONS

We acquired imaging polarimetry of 68 SNe Ia with the FOcal Reducer and low dispersion Spectrograph (FORS2; Appenzeller et al. 1998) mounted at the European Southern Observatory's *Very Large Telescope* (ESO's *VLT*). The SNe were observed during the interval 2018–2021 (ESO observing periods P101, P102, and P104) to create a statistical sample of SN Ia polarization measurements (Prog. IDs 0101.D-0190(A), 0102.D-0163(A), and 0104.D-0175(A), PI Cikota). Additionally, we included the complete sample of 35 archival SNe Ia from Cikota et al. (2019) that were observed with FORS1/2 in spectropolarimetry mode between 2001 and 2015.

2.1 Target selection

Every year hundreds of SNe Ia are being discovered by transient surveys such as the Zwicky Transient Facility (ZTF; Bellm et al. 2019), Pan-STARRS (Chambers et al. 2016), and *GAIA* (Gaia Collaboration 2016), and classified by follow-up surveys such as the Public ESO Spectroscopic Survey for Transient Objects (PESSTO; Smartt et al. 2015). For instance, there were 420 SNe Ia discovered in 2016 (according to the Transient Name Server; TNS)[1]. Of these, 210 were brighter than 18 mag at peak, and 106 were brighter than 17 mag. For this experiment we have been monitoring the TNS and the Latest Supernovae Page[2] for recently classified SNe, visible from the Southern hemisphere, and selected the brightest ($m_V \lesssim 18$ mag) SNe Ia that exploded in the most nearby host galaxies of any morphological type.

2.2 Observing strategy

SNe Ia brighter than $m_V \approx 18$ mag were observed in imaging polarimetry mode through the B filter, and the data were instantaneously reduced. If an observation toward a SN Ia showed significant polarization ($p \gtrsim 1.0$ per cent in P101 and P102; $p \gtrsim 0.5$ per cent in P104), we observed the SN additionally in the V band, to determine the slope of the polarization curve. The reason that we lowered the follow-up condition from $p \approx 1.0$ per cent in P101 and P102 to $p \approx 0.5$ per cent in P104 was to increase the sample of SNe for which we know the slope of the polarization curves. During P101
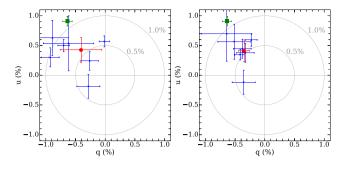
Figure 2. Interstellar polarization estimate using field stars in the case of SN 2018koy. The small blue dots are the individual field-star measurements, and the large red dot shows their weighted mean. The green square displays the polarization of SN 2018koy. The left plot shows the Stokes q and u parameter measurements uncorrected for instrumental polarization, and on the right, the same measurements are shown after correcting for the instrumental polarization.

and P102, only three out of 42 observed SNe displayed polarization values higher than 1 per cent, and six additional SNe had polarization values between 0.5 per cent and 1 per cent in the B band. However, based on the sample of Zelaya et al. (2017), we initially expected that ∼1/3 of SNe will have polarization values higher than 1 per cent in the B band.

Observations in B ($\lambda_{eff} = 440$ nm) and V ($\lambda_{eff} = 557$ nm) are sufficient to determine whether the polarization curve is 'normal' or steeply rising toward the blue (see e.g. Fig. 2 of Patat et al. 2015, and the determination of the slope by Zelaya et al. 2017, their fig. 2). The observing log is presented in Table 1. For 12 SNe we conducted follow-up observations in the V band. SN 2019vv was mistakenly observed only in the V band (instead of in the B band).

3 DATA REDUCTION AND METHODS

3.1 Imaging polarimetry

The imaging polarimetry mode of FORS2 (Appenzeller et al. 1998) splits the image through a Wollaston prism into two beams with perpendicular polarizations: the ordinary (o) beam and the extraordinary (e) beam. The multi-object spectroscopy (MOS) slitlets strip mask prevents overlaps of the split beams. The targets were observed in the upper frame (CHIP1) centred on the optical axis of the telescope. The polarization is determined by conducting aperture photometry of the target in the ordinary and extraordinary beams using the DAOPHOT.PHOT package (Stetson 1987) in IRAF. The normalized Stokes parameters (q and u) were calculated following the FORS2 User Manual (ESO 2015) using the Fourier transform of the normalized flux differences measured at four half-wave retarder plate angles (θ) of $0°$, $22.5°$, $45°$, and $67.5°$ (equation 1):

$$q = \frac{2}{N} \sum_{i=0}^{N-1} F(\theta_i) \cos(4\theta_i),$$
$$u = \frac{2}{N} \sum_{i=0}^{N-1} F(\theta_i) \sin(4\theta_i). \tag{1}$$

$F(\theta_i)$ is the normalized flux difference between the ordinary (f^o) and extraordinary (f^e) beams (equation 2),

$$F(\theta_i) = \frac{f^o(\theta_i) - f^e(\theta_i)}{f^o(\theta_i) + f^e(\theta_i)}. \tag{2}$$

In equation (1), N ranges over the aforementioned half-wave retarder plate angles, $\theta_i = 22.5° \times i$, with $0 \leq i \leq 3$.

Table 1. Observing log of the imaging polarization survey. The dates denote the beginning of the observations. The right ascension (α) and declination (δ) are remeasured SN coordinates.

SN name	UT Date	α(J2000)	δ(J2000)	Band	Exposure (s)
SN 2018cif	2018-06-13 06:56	22 03 00.94	+02 35 52.0	b_HIGH	4 × 110
SN 2018cif	2018-06-13 07:10	22 03 00.94	+02 35 52.0	v_HIGH	4 × 56
SN 2018evt	2019-01-09 08:26	13 46 39.17	−09 38 35.9	b_HIGH	4 × 120
SN 2018fhw	2018-09-07 06:27	04 18 06.18	−63 36 56.5	b_HIGH	4 × 276
SN 2018fhx	2018-09-08 08:23	06 24 37.99	−23 43 59.0	b_HIGH	4 × 500
SN 2018fnq	2018-09-09 00:00	20 12 29.98	−44 06 35.3	b_HIGH	4 × 65
SN 2018fnq	2018-09-11 00:10	20 12 29.98	−44 06 35.3	v_HIGH	4 × 28
SN 2018fqd	2018-09-09 00:13	20 51 51.42	−36 50 11.7	b_HIGH	4 × 180
SN 2018fqn	2018-09-09 00:41	22 39 38.18	−15 05 09.8	b_HIGH	4 × 350
SN 2018fsa	2018-09-08 05:42	22 25 37.04	−13 04 30.0	b_HIGH	4 × 110
SN 2018fuk	2018-09-09 08:58	05 45 07.11	−79 23 48.2	b_HIGH	4 × 200
SN 2018fvi	2018-09-08 06:02	01 57 42.52	−67 11 14.0	b_HIGH	4 × 110
SN 2018fvi	2018-09-09 04:57	01 57 42.52	−67 11 14.0	v_HIGH	4 × 250
SN 2018fvy	2018-09-09 04:04	01 32 16.22	−33 06 05.3	b_HIGH	4 × 280
SN 2018fzm	2018-09-11 00:25	21 03 19.85	−51 32 47.8	b_HIGH	4 × 200
SN 2018gyr	2018-10-06 00:08	00 49 47.12	−61 39 13.1	b_HIGH	4 × ∼850
SN 2018hsa	2018-11-09 00:25	21 15 01.08	−47 12 36.9	b_HIGH	4 × ∼60
SN 2018hsy	2018-11-06 08:15	09 30 29.83	+16 20 37.3	b_HIGH	4 × 142
SN 2018hts	2018-11-06 01:44	23 24 32.94	+17 05 37.9	b_HIGH	4 × 300
SN 2018htt	2018-11-14 04:17	03 06 02.90	−15 36 41.3	b_HIGH	4 × 8
SN 2018jbm	2018-12-03 04:07	01 42 17.65	−45 24 52.1	b_HIGH	4 × 200
SN 2018jdq	2018-12-06 07:48	11 25 25.69	−08 27 59.1	b_HIGH	4 × 77
SN 2018jeo	2018-12-03 07:57	09 04 36.91	−19 47 09.7	b_HIGH	4 × 90
SN 2018jff	2018-12-05 01:11	23 48 06.40	−44 58 48.7	b_HIGH	4 × 550
SN 2018jgn	2018-12-06 02:36	00 02 55.85	−26 54 51.5	b_HIGH	4 × 230
SN 2018jky	2018-12-09 00:58	03 26 02.12	−17 33 46.3	b_HIGH	4 × 142, 2 × 90, 6 × 60, 4 × 70
SN 2018jny	2018-12-11 06:43	09 24 37.76	+25 23 42.7	b_HIGH	8 × ∼200
SN 2018jrn	2018-12-14 07:52	12 52 35.42	−21 54 56.6	b_HIGH	4 × ∼300
SN 2018jtj	2019-01-08 08:13	12 41 03.39	+08 04 21.8	b_HIGH	4 × 462
SN 2018kav	2019-01-04 01:23	04 50 54.70	−17 59 11.5	b_HIGH	4 × 230
SN 2018koy	2019-01-04 01:48	05 41 13.76	−13 13 27.1	b_HIGH	4 × 276
SN 2018koy	2019-01-05 01:21	05 41 13.76	−13 13 27.1	v_HIGH	4 × 90
SN 2018kyi	2019-01-05 04:00	07 07 09.50	+26 19 29.7	b_HIGH	4 × 142
SN 2019axg	2019-03-06 05:12	10 36 36.18	−07 06 32.2	b_HIGH	4 × 225
SN 2019bak	2019-03-06 04:24	10 13 31.79	+29 33 05.4	b_HIGH	4 × 400
SN 2019baq	2019-03-06 07:33	12 22 01.42	+20 20 27.4	b_HIGH	4 × 120
SN 2019bdz	2019-03-06 06:56	14 48 36.92	+06 48 52.2	b_HIGH	4 × 105
SN 2019bff	2019-03-08 06:59	14 14 31.78	+17 13 58.7	b_HIGH	4 × 120
SN 2019bjw	2019-03-05 07:05	10 55 47.44	+27 40 17.1	b_HIGH	4 × 142
SN 2019bjz	2019-03-05 08:11	16 02 11.80	+15 55 05.8	b_HIGH	4 × 77
SN 2019bkh	2019-03-05 08:28	13 08 57.41	+28 16 52.1	b_HIGH	4 × 142
SN 2019bpb	2019-03-12 01:50	05 12 09.87	−43 55 16.6	b_HIGH	4 × ∼ 400
SN 2019kg	2019-02-06 04:08	11 42 45.75	+21 42 53.9	b_HIGH	4 × 142
SN 2019np	2019-01-13 06:47	10 29 21.97	+29 30 38.5	b_HIGH	4 × 50
SN 2019rm	2019-01-29 03:26	05 53 13.28	−73 06 56.9	b_HIGH	4 × 180
SN 2019rx	2019-01-29 01:56	05 21 59.63	−07 11 24.7	b_HIGH	4 × ∼480
SN 2019rzm	2019-10-23 02:24	01 17 21.66	−16 04 04.7	b_HIGH	4 × 120
SN 2019shq	2019-10-24 08:26	08 44 28.67	−31 41 25.6	b_HIGH	4 × 142
SN 2019ubs	2019-11-24 01:45	02 26 24.11	+28 30 28.8	b_HIGH	4 × 450
SN 2019ubs	2019-11-27 01:24	02 26 24.11	+28 30 28.8	v_HIGH	4 × 100
SN 2019ubt	2019-11-23 02:15	23 29 57.48	+29 49 46.5	b_HIGH	4 × 750
SN 2019udk	2019-11-25 02:13	00 40 51.25	+02 50 25.4	b_HIGH	4 × 100
SN 2019udk	2019-11-27 01:05	00 40 51.25	+02 50 25.4	v_HIGH	4 × 40
SN 2019uhz	2019-11-23 03:20	01 47 13.94	−08 27 40.4	b_HIGH	4 × 260
SN 2019ujy	2019-11-23 00:44	19 41 54.67	−20 10 04.8	b_HIGH	4 × 550
SN 2019ulp	2019-11-25 05:56	08 28 13.09	+00 01 29.7	b_HIGH	4 × 150
SN 2019umr	2019-11-25 01:26	22 16 04.96	−26 40 41.9	b_HIGH	4 × 67
SN 2019umr	2019-11-27 00:35	22 16 04.96	−26 40 41.9	v_HIGH	4 × 25
SN 2019uoo	2019-11-24 07:15	08 38 45.65	−14 40 49.1	b_HIGH	4 × 350
SN 2019upw	2019-11-25 01:50	00 26 15.49	+21 48 36.4	b_HIGH	8 × 60
SN 2019upw	2019-11-27 00:52	00 26 15.49	+21 48 36.4	v_HIGH	4 × 20
SN 2019urn	2019-11-24 00:35	00 57 49.26	−17 38 27.0	b_HIGH	4 × 300
SN 2019vju	2019-12-24 07:44	11 04 00.26	−18 46 35.7	b_HIGH	4 × 500
SN 2019vnj	2019-12-21 07:46	11 09 01.21	−14 38 10.1	b_HIGH	4 × 196

Table 1 – *continued*

SN name	UT Date	α(J2000)	δ(J2000)	Band	Exposure (s)
SN 2019vrq	2020-02-22 00:53	03 04 21.49	−16 01 25.4	b_HIGH	4×200, 4×280
SN 2019vsa	2019-12-26 07:08	12 05 47.59	−27 56 37.6	b_HIGH	4×160
SN 2019vsa	2019-12-27 07:21	12 05 47.59	−27 56 37.6	v_HIGH	4×20
SN 2019vv	2019-02-06 07:58	15 34 03.66	+02 12 40.4	v_HIGH	4×169
SN 2019wka	2019-12-27 01:58	03 14 40.13	−00 52 16.9	b_HIGH	4×77
SN 2019wqz	2019-12-27 06:40	11 47 18.38	−29 11 19.7	b_HIGH	4×77
SN 2020bpz	2020-02-22 07:18	11 40 58.53	−11 26 57.3	b_HIGH	4×276
SN 2020ckp	2020-02-22 02:08	08 36 21.31	−25 31 57.9	b_HIGH	4×142, 4×300
SN 2020ckp	2020-02-23 06:18	08 36 21.31	−25 31 57.9	v_HIGH	4×200
SN 2020clq	2020-02-22 01:47	04 33 25.53	−04 15 57.7	b_HIGH	4×35
SN 2020cpt	2020-02-24 08:12	14 57 30.26	+08 23 24.4	b_HIGH	4×160
SN 2020ctr	2020-02-22 02:58	08 58 37.58	+20 11 31.1	b_HIGH	4×110, 4×200
SN 2020dvr	2020-03-20 01:54	09 54 35.14	−19 53 14.7	b_HIGH	4×12
SN 2020dyf	2020-03-20 07:54	15 30 29.68	−12 36 06.1	b_HIGH	4×100
SN 2020dyf	2020-03-22 07:20	15 30 29.68	−12 36 06.1	v_HIGH	4×42
SN 2020ejm	2020-03-20 06:15	10 16 18.74	−33 33 49.7	b_HIGH	4×18
SN 2020ejm	2020-03-21 03:26	10 16 18.74	−33 33 49.7	v_HIGH	8×4

The normalized Stokes parameters were corrected for the residual retardance chromatism from the superachromatic half-wave plate, using the wavelength-dependent retardance offset, $\Delta\theta(\lambda)$, tabulated in ESO (2015),

$$q_0 = q \cos 2\Delta\theta(\lambda) - u \sin 2\Delta\theta(\lambda),$$
$$u_0 = q \cos 2\Delta\theta(\lambda) + u \sin 2\Delta\theta(\lambda). \quad (3)$$

Finally, the polarization is calculated as

$$p = \sqrt{q_0^2 + u_0^2} \quad (4)$$

and the polarization angle as

$$\theta_0 = \frac{1}{2} \arctan \frac{u_0}{q_0}. \quad (5)$$

The uncertainties in the normalized flux differences, the normalized Stokes parameters, and the polarization per cent and angle were calculated by propagating the flux uncertainty of the aperture-photometry measured in the ordinary and extraordinary beams, which were extracted along with the flux measurements. The polarization bias was corrected following equation (3) of Wang, Wheeler & Höflich (1997a).

The imaging-polarimetry results in the *B* and *V* bands are listed in Table 2. Furthermore, we calculated the average Stokes *q* and *u* in the *B* (4000–4800 Å) and *V* (5200–6000 Å) bands for the 35 archival SNe observed in spectropolarimetry mode and published by Cikota et al. (2019). The polarization measurements of these SNe are included in the analysis in this work and given in Table 3.

3.2 Interstellar polarization removal

We estimated the MW interstellar polarization (ISP) along the sight-lines toward the SNe Ia using field stars in the imaging-polarimetry data. Using SEXTRACTOR (Bertin & Arnouts 1996), we extracted all stars in the field with a 'detection threshold' >50 standard deviations of the background noise and selected those with 'ellipticity' <0.3 and 'flags' <1. This excludes (i) galaxies and unreliable objects with neighbours that are bright and close enough to significantly bias the photometry, (ii) objects originally blended with another one, (iii) saturated objects, (iv) truncated objects, or (v) objects with incomplete or corrupt aperture data. We measured the flux of the selected stars in the ordinary and extraordinary beams using

IRAF's DAOPHOT.PHOT package and calculated the polarization as described in Section 3.1.

There is strong linear instrumental polarization across the FORS2 field, which shows a high degree of axial symmetry and increases from <0.03 per cent on the optical axis to ∼1.4 per cent at the edges of the field (Patat & Romaniello 2006). The instrumental polarization is well characterized, within 0.05 per cent of the absolute value (Patat & Romaniello 2006). To correct for the instrumental polarization we apply a cubic polynomial of the degree of polarization as a function of the distance from the optical axis determined by González-Gaitán et al. (2020)

$$p_{B_{\text{inst}}}(r) = \left(1.114 \times 10^{-5}\right) r - \left(1.275 \times 10^{-8}\right) r^2 \quad (6)$$
$$+ \left(9.153 \times 10^{-12}\right) r^3,$$

and estimate the polarization angle as

$$\alpha = \arctan((y - y_c)/(x - x_c)), \quad (7)$$

where $p_{B_{\text{inst}}}$ is the instrumental polarization in the *B* band, *r* is the distance from the optical axis (x_c, y_c), and (x, y) are the stellar coordinates in pixels.

An example of field stars before and after correcting for the instrumental polarization is shown in Fig. 2. By determining the weighted mean of these field stars in the *q–u* plane, we estimate the average interstellar polarization (produced by MW dust) for each field. The uncertainty of the average ISP is typically ∼0.3–0.5 per cent and varies from field to field, depending on the scatter and number of individually measured stars. We finally inspect the *q–u* plots (e.g. shown in Fig. 2) and in the case of significant ISP subtract the average interstellar polarization from the SN polarization measurements

$$q_{\text{SN}} = q_0 - q_{\text{ISP}},$$
$$u_{\text{SN}} = u_0 - u_{\text{ISP}}. \quad (8)$$

The estimated average value of the interstellar polarization for a field is often close to the measured polarization of the SN or located in the same quadrant in the *q–u* plane, as shown in Fig. 2 for the case of SN 2018koy. If there is only one field star, or 2–3 field stars with inconsistent measurements in the *q–u* plane, we skip the ISP correction. Furthermore, if the average ISP is close to zero and has large error bars, to avoid introducing unnecessary systematic errors,

Table 2. Polarization measurements of 69 SNe Ia in the *B* band obtained in this work. 12 SNe have been followed-up in the *V* band.

Name	Filter	q (per cent)	u (per cent)	$\theta(°)$	p (per cent)	q_{ISP} (per cent)	u_{ISP} (per cent)	p_{ISP} (per cent)	ISPcorr	p_{corr} (per cent)
				SNe Ia in spiral host galaxies						
SN 2018cif	B	0.05 ± 0.07	0.06 ± 0.07	25.1 ± 25.7	0.08 ± 0.07	0.0 ± 0.14	-0.34 ± 0.38	0.34 ± 0.38	No	0.02 ± 0.07
SN 2018cif	V	-0.02 ± 0.09	0.11 ± 0.09	51.2 ± 23.0	0.12 ± 0.09	...	...	...	No	0.04 ± 0.09
SN 2018fqd	B	0.06 ± 0.22	-0.73 ± 0.25	137.3 ± 9.8	0.73 ± 0.25	0.31 ± 0.18	-0.2 ± 0.16	0.37 ± 0.17	Yes	0.44 ± 0.29
SN 2018fuk	B	0.04 ± 0.05	0.13 ± 0.05	36.4 ± 10.5	0.14 ± 0.05	0.54 ± 0.27	0.02 ± 0.22	0.54 ± 0.27	No	0.12 ± 0.05
SN 2018fvi	B	-0.2 ± 0.16	0.78 ± 0.16	52.2 ± 5.7	0.81 ± 0.16	0.07 ± 0.14	-0.25 ± 0.17	0.26 ± 0.17	No	0.77 ± 0.16
SN 2018fvi	V	-0.56 ± 0.08	0.19 ± 0.08	80.6 ± 4.1	0.59 ± 0.08	...	...	...	No	0.58 ± 0.08
SN 2018fvy	B	-0.06 ± 0.09	-0.07 ± 0.08	114.7 ± 26.2	0.09 ± 0.08	...	...	...	No	0.01 ± 0.08
SN 2018fzm	B	0.03 ± 0.12	-0.27 ± 0.12	138.2 ± 12.7	0.27 ± 0.12	0.17 ± 0.17	-0.42 ± 0.3	0.45 ± 0.29	Yes	0.0 ± 0.28
SN 2018hsa	B	0.16 ± 0.06	-0.39 ± 0.05	146.2 ± 3.5	0.42 ± 0.05	0.38 ± 0.21	-0.35 ± 0.04	0.52 ± 0.16	Yes	0.02 ± 0.22
SN 2018hsy	B	-0.57 ± 0.12	-0.27 ± 0.13	102.7 ± 5.5	0.63 ± 0.12	-0.28 ± 0.01	-0.2 ± 0.06	0.34 ± 0.04	Yes	0.25 ± 0.12
SN 2018jbm	B	-0.05 ± 0.1	0.2 ± 0.1	52.0 ± 13.9	0.21 ± 0.1	0.0 ± 0.09	0.3 ± 0.09	0.3 ± 0.09	Yes	0.0 ± 0.13
SN 2018jdq	B	0.39 ± 0.06	0.07 ± 0.06	5.1 ± 4.3	0.4 ± 0.06	0.24 ± 0.12	0.09 ± 0.12	0.26 ± 0.12	Yes	0.03 ± 0.13
SN 2018jeo	B	0.0 ± 0.05	-0.1 ± 0.05	135.0 ± 14.3	0.1 ± 0.05	-0.02 ± 0.35	-0.11 ± 0.17	0.11 ± 0.18	Yes	0.0 ± 0.33
SN 2018jff	B	-0.1 ± 0.06	0.08 ± 0.06	70.7 ± 13.4	0.13 ± 0.06	-0.13 ± 0.14	0.17 ± 0.14	0.21 ± 0.14	Yes	0.0 ± 0.15
SN 2018jky	B	0.33 ± 0.03	0.08 ± 0.03	6.8 ± 2.5	0.34 ± 0.03	0.09 ± 0.05	-0.18 ± 0.05	0.2 ± 0.05	No	0.34 ± 0.03
SN 2018jny	B	-0.07 ± 0.06	-0.29 ± 0.06	128.2 ± 5.8	0.3 ± 0.06	0.12 ± 0.05	0.11 ± 0.06	0.16 ± 0.05	No	0.29 ± 0.06
SN 2018jtj	B	-0.03 ± 0.07	-0.22 ± 0.07	131.1 ± 9.0	0.22 ± 0.07	-0.56 ± 0.08	0.08 ± 0.07	0.57 ± 0.08	No	0.2 ± 0.07
SN 2018kav	B	-0.18 ± 0.1	0.2 ± 0.1	66.0 ± 10.6	0.27 ± 0.1	0.04 ± 0.06	0.17 ± 0.1	0.17 ± 0.1	Yes	0.16 ± 0.12
SN 2019axg	B	-0.65 ± 0.2	0.68 ± 0.2	66.9 ± 6.1	0.94 ± 0.2	0.07 ± 0.09	0.13 ± 0.16	0.15 ± 0.15	Yes	0.85 ± 0.23
SN 2019bak	B	0.17 ± 0.17	-0.04 ± 0.17	173.4 ± 27.9	0.17 ± 0.17	0.42 ± 0.11	0.06 ± 0.54	0.42 ± 0.13	No	0.01 ± 0.17
SN 2019bdz	B	0.09 ± 0.09	0.3 ± 0.09	36.7 ± 8.2	0.31 ± 0.09	-0.05 ± 0.13	0.2 ± 0.06	0.21 ± 0.07	Yes	0.05 ± 0.14
SN 2019bff	B	-0.05 ± 0.12	0.91 ± 0.12	46.6 ± 3.8	0.91 ± 0.12	-0.17 ± 0.27	0.17 ± 0.06	0.24 ± 0.2	Yes	0.72 ± 0.14
SN 2019bjw	B	0.14 ± 0.07	-0.02 ± 0.07	175.9 ± 14.2	0.14 ± 0.07	-0.04 ± 0.02	-0.01 ± 0.07	0.04 ± 0.03	No	0.11 ± 0.07
SN 2019bkh	B	-0.11 ± 0.12	-0.11 ± 0.12	112.5 ± 22.1	0.16 ± 0.12	0.05 ± 0.06	-0.02 ± 0.03	0.05 ± 0.06	No	0.06 ± 0.12
SN 2019np	B	-0.03 ± 0.07	0.42 ± 0.07	47.0 ± 4.8	0.42 ± 0.07	...	...	...	No	0.41 ± 0.07
SN 2019rx	B	-0.21 ± 0.14	-0.14 ± 0.11	106.8 ± 14.9	0.25 ± 0.13	-0.17 ± 0.06	0.17 ± 0.17	0.24 ± 0.13	No	0.18 ± 0.13
SN 2019shq	B	-0.41 ± 0.36	0.25 ± 0.37	74.3 ± 21.6	0.48 ± 0.36	-0.46 ± 0.18	-0.06 ± 0.17	0.46 ± 0.18	Yes	0.0 ± 0.41
SN 2019ubs	B	0.11 ± 0.06	-0.72 ± 0.06	139.3 ± 2.4	0.73 ± 0.06	-0.19 ± 0.29	-0.72 ± 0.07	0.74 ± 0.1	Yes	0.01 ± 0.3
SN 2019ubs	V	0.01 ± 0.11	-0.66 ± 0.11	135.4 ± 4.8	0.66 ± 0.11	...	...	...	No	0.65 ± 0.11
SN 2019ubt	B	-0.19 ± 0.09	0.67 ± 0.1	52.9 ± 4.1	0.7 ± 0.1	...	...	...	No	0.68 ± 0.1
SN 2019udk	B	-1.69 ± 0.17	-0.75 ± 0.16	102.0 ± 2.6	1.85 ± 0.17	-0.08 ± 0.24	-0.14 ± 0.23	0.16 ± 0.23	Yes	1.67 ± 0.29
SN 2019udk	V	-1.47 ± 0.16	-0.55 ± 0.16	100.3 ± 2.9	1.57 ± 0.16	...	...	...	No	1.56 ± 0.16
SN 2019uhz	B	-0.04 ± 0.11	-0.39 ± 0.11	132.1 ± 8.0	0.39 ± 0.11	-0.56 ± 0.26	0.73 ± 0.68	0.92 ± 0.56	No	0.36 ± 0.11
SN 2019ulp	B	0.11 ± 0.13	-0.27 ± 0.13	146.1 ± 12.8	0.29 ± 0.13	-0.08 ± 0.06	0.18 ± 0.08	0.2 ± 0.08	No	0.23 ± 0.13
SN 2019umr	B	-0.29 ± 0.22	0.78 ± 0.22	55.2 ± 7.6	0.83 ± 0.22	-0.02 ± 0.15	-0.05 ± 0.06	0.05 ± 0.08	No	0.77 ± 0.22
SN 2019umr	V	-0.4 ± 0.23	0.57 ± 0.23	62.5 ± 9.7	0.69 ± 0.23	...	...	...	No	0.61 ± 0.23
SN 2019upw	B	-0.47 ± 0.05	-0.36 ± 0.05	108.7 ± 2.4	0.59 ± 0.05	...	...	...	No	0.59 ± 0.05
SN 2019upw	V	-0.54 ± 0.11	-0.25 ± 0.11	102.5 ± 5.1	0.6 ± 0.11	...	...	...	No	0.58 ± 0.11
SN 2019vju	B	-0.46 ± 0.36	-0.21 ± 0.36	102.3 ± 20.4	0.51 ± 0.36	0.01 ± 0.14	-0.03 ± 0.03	0.03 ± 0.05	Yes	0.21 ± 0.38
SN 2019vnj	B	-0.03 ± 0.13	0.15 ± 0.13	50.7 ± 24.3	0.15 ± 0.13	...	...	...	No	0.04 ± 0.13
SN 2019vrq	B	0.29 ± 0.1	-0.05 ± 0.1	175.1 ± 9.7	0.29 ± 0.1	0.41 ± 0.12	-0.14 ± 0.04	0.43 ± 0.11	Yes	0.02 ± 0.14
SN 2019vsa	B	-0.32 ± 0.12	-0.63 ± 0.12	121.5 ± 4.9	0.71 ± 0.12	-0.17 ± 0.26	0.13 ± 0.17	0.21 ± 0.23	No	0.69 ± 0.12
SN 2019vsa	V	-0.43 ± 0.1	-0.7 ± 0.1	119.0 ± 3.6	0.82 ± 0.1	...	...	...	No	0.81 ± 0.1
SN 2019wka	B	0.45 ± 0.1	0.03 ± 0.1	1.9 ± 6.4	0.45 ± 0.1	0.55 ± 0.07	0.06 ± 0.1	0.55 ± 0.07	Yes	0.0 ± 0.12
SN 2019wqz	B	-0.08 ± 0.08	-0.07 ± 0.08	110.6 ± 21.6	0.11 ± 0.08	-0.12 ± 0.11	0.22 ± 0.12	0.25 ± 0.12	No	0.05 ± 0.08
SN 2020bpz	B	-0.01 ± 0.08	0.03 ± 0.08	54.2 ± 72.5	0.03 ± 0.08	...	...	...	No	0.0 ± 0.08
SN 2020ckp	B	-0.17 ± 0.13	-0.93 ± 0.13	129.8 ± 3.9	0.95 ± 0.13	-0.22 ± 0.14	-0.89 ± 0.18	0.92 ± 0.18	Yes	0.0 ± 0.2
SN 2020ckp	V	-0.23 ± 0.22	-0.86 ± 0.23	127.6 ± 7.2	0.89 ± 0.23	...	...	...	No	0.83 ± 0.23
SN 2020dvr	B	-0.04 ± 0.09	-0.08 ± 0.09	121.7 ± 28.8	0.09 ± 0.09	0.08 ± 0.12	0.22 ± 0.23	0.23 ± 0.22	No	0.0 ± 0.09
SN 2020dyf	B	-0.57 ± 0.06	1.12 ± 0.06	58.5 ± 1.4	1.26 ± 0.06	-0.87 ± 0.28	1.31 ± 0.19	1.57 ± 0.22	Yes	0.16 ± 0.26
SN 2020dyf	V	-0.81 ± 0.08	1.12 ± 0.08	63.0 ± 1.6	1.38 ± 0.08	...	...	...	No	1.38 ± 0.08
SN 2020ejm	B	-0.5 ± 0.07	0.59 ± 0.07	65.1 ± 2.6	0.77 ± 0.07	-0.43 ± 0.06	0.35 ± 0.06	0.55 ± 0.06	Yes	0.22 ± 0.09
SN 2020ejm	V	-0.39 ± 0.13	0.54 ± 0.13	63.1 ± 5.7	0.66 ± 0.13	...	...	...	No	0.64 ± 0.13
				SNe Ia in elliptical host galaxies						
SN 2018fhw	B	-0.06 ± 0.11	-0.14 ± 0.11	123.4 ± 20.7	0.15 ± 0.11	-0.11 ± 0.16	-0.09 ± 0.18	0.14 ± 0.17	Yes	0.0 ± 0.2
SN 2018htt	B	0.28 ± 0.08	-0.05 ± 0.08	174.9 ± 8.1	0.28 ± 0.08	0.36 ± 0.09	-0.09 ± 0.19	0.37 ± 0.1	Yes	0.0 ± 0.14
SN 2018jgn	B	-0.34 ± 0.41	0.1 ± 0.11	81.8 ± 31.9	0.35 ± 0.39	...	...	...	No	0.0 ± 0.39
SN 2018jrn	B	0.24 ± 0.07	0.02 ± 0.1	2.4 ± 8.4	0.24 ± 0.07	...	...	...	No	0.22 ± 0.07
SN 2019baq	B	-0.05 ± 0.09	0.2 ± 0.09	52.0 ± 12.5	0.21 ± 0.09	0.1 ± 0.06	0.08 ± 0.09	0.13 ± 0.07	Yes	0.12 ± 0.12
SN 2019bjz	B	-0.37 ± 0.13	0.13 ± 0.13	80.3 ± 9.5	0.39 ± 0.13	-0.02 ± 0.09	0.13 ± 0.17	0.13 ± 0.17	Yes	0.28 ± 0.16
SN 2019ujy	B	0.71 ± 0.09	-0.03 ± 0.09	178.8 ± 3.6	0.71 ± 0.09	0.74 ± 0.28	-0.09 ± 0.18	0.75 ± 0.28	Yes	-0.0 ± 0.22
SN 2019urn	B	0.11 ± 0.06	0.08 ± 0.06	18.0 ± 12.6	0.14 ± 0.06	-0.06 ± 0.07	0.07 ± 0.07	0.09 ± 0.07	No	0.11 ± 0.06

Table 2 – *continued*

Name	Filter	q (per cent)	u (per cent)	$\theta(°)$	p (per cent)	q_{ISP} (per cent)	u_{ISP} (per cent)	p_{ISP} (per cent)	ISPcorr	p_{corr} (per cent)
SN 2020cpt	B	−0.01 ± 0.13	0.17 ± 0.13	46.7 ± 21.9	0.17 ± 0.13	−0.28 ± 0.19	0.18 ± 0.19	0.33 ± 0.19	No	0.07 ± 0.13
SN 2020ctr	B	−0.01 ± 0.06	0.21 ± 0.06	46.4 ± 8.2	0.21 ± 0.06	−0.09 ± 0.09	0.0 ± 0.1	0.09 ± 0.09	No	0.19 ± 0.06
SNe Ia in S0 host galaxies										
SN 2018evt	B	−1.37 ± 0.09	−0.32 ± 0.09	96.6 ± 1.8	1.41 ± 0.09	−0.29 ± 0.21	0.0 ± 0.07	0.29 ± 0.21	Yes	1.08 ± 0.22
SN 2018fhx	B	0.2 ± 0.35	−0.06 ± 0.36	171.7 ± 48.1	0.21 ± 0.35	−0.01 ± 0.68	−0.29 ± 0.29	0.29 ± 0.29	No	0.0 ± 0.35
SN 2018fnq	B	1.67 ± 0.06	−0.32 ± 0.06	174.6 ± 1.0	1.7 ± 0.06	0.37 ± 0.19	−0.22 ± 0.13	0.43 ± 0.18	Yes	1.27 ± 0.2
SN 2018fnq	V	0.07 ± 0.07	−0.22 ± 0.07	144.3 ± 8.9	0.24 ± 0.07	...	...	...	No	0.21 ± 0.07
SN 2018gyr	B	−0.16 ± 0.18	0.01 ± 0.18	88.2 ± 32.2	0.16 ± 0.18	...	...	...	No	0.0 ± 0.18
SN 2019rzm	B	−0.23 ± 0.08	0.07 ± 0.08	81.5 ± 9.5	0.24 ± 0.08	0.03 ± 0.1	−0.19 ± 0.1	0.19 ± 0.1	No	0.21 ± 0.08
SN 2019uoo	B	0.12 ± 0.31	0.0 ± 0.31	0.0 ± 74.0	0.12 ± 0.31	0.31 ± 0.24	−0.12 ± 0.11	0.33 ± 0.23	No	0.0 ± 0.31
SN 2019vv	V	−0.11 ± 0.27	0.62 ± 0.29	50.2 ± 13.2	0.63 ± 0.29	...	...	...	No	0.49 ± 0.29
SN 2020clq	B	−0.36 ± 0.07	0.16 ± 0.07	78.0 ± 5.1	0.39 ± 0.07	0.25 ± 0.02	−0.06 ± 0.05	0.26 ± 0.02	No	0.38 ± 0.07
SNe Ia in irregular host galaxies										
SN 2019rm	B	0.5 ± 0.05	0.41 ± 0.05	19.7 ± 2.2	0.65 ± 0.05	0.5 ± 0.12	0.4 ± 0.13	0.64 ± 0.12	Yes	0.0 ± 0.14
SNe Ia in host galaxies of unknown morphological classification										
SN 2018fqn	B	0.12 ± 0.05	0.0 ± 0.05	0.0 ± 11.9	0.12 ± 0.05	0.18 ± 0.3	0.0 ± 0.3	0.18 ± 0.3	Yes	0.0 ± 0.3
SN 2018fsa	B	0.2 ± 0.08	0.36 ± 0.08	30.5 ± 5.6	0.41 ± 0.08	...	...	...	No	0.4 ± 0.08
SN 2018hts	B	−0.29 ± 0.05	−0.1 ± 0.05	99.5 ± 4.7	0.31 ± 0.05	−0.15 ± 0.05	−0.19 ± 0.01	0.24 ± 0.03	Yes	0.14 ± 0.07
SN 2018koy	B	−0.64 ± 0.08	0.91 ± 0.08	62.6 ± 2.1	1.11 ± 0.08	−0.35 ± 0.08	0.45 ± 0.14	0.57 ± 0.12	Yes	0.5 ± 0.14
SN 2018koy	V	−0.66 ± 0.08	0.9 ± 0.08	63.0 ± 2.0	1.12 ± 0.08	...	...	...	No	1.11 ± 0.08
SN 2018kyi	B	0.0 ± 0.06	−0.31 ± 0.06	135.0 ± 5.5	0.31 ± 0.06	0.08 ± 0.15	−0.36 ± 0.15	0.37 ± 0.15	Yes	0.0 ± 0.16
SN 2019bpb	B	0.04 ± 0.07	−0.3 ± 0.07	138.8 ± 6.6	0.3 ± 0.07	0.0 ± 0.01	0.15 ± 0.13	0.15 ± 0.13	No	0.29 ± 0.07
SN 2019kg	B	0.76 ± 0.11	−0.08 ± 0.11	177.0 ± 4.1	0.76 ± 0.11	0.03 ± 0.25	0.11 ± 0.25	0.11 ± 0.25	Yes	0.66 ± 0.27

SN 2019vv has been observed in *V* band only. p_{corr} are the ISP subtracted (if so indicated in the ISP$_{corr}$) and polarization bias corrected values.

we also do not subtract the ISP. We indicate in Table 2 ('ISPcorr' column) whether the ISP has been subtracted.

3.3 Normalized SN position

We determined the normalized distances of the SNe from their host galaxy centres in terms of flux percentile of the total host galaxy flux. This can be achieved by fitting elliptical isophotes to the host galaxies (Jedrzejewski 1987) and determining the flux value contained inside of the ellipse containing the SN. This value we then compared to the total flux of the galaxy and calculated the flux percentile.

To cross-match our SN sample to host galaxies, we queried our sample in the TNS for listed host galaxies. For those SNe with listed host galaxies, the host-galaxy coordinates, redshifts, and morphological classifications were acquired directly from the NASA/IPAC Extragalactic Database (NED; Helou et al. 1991), or if the information was not available in NED, cross-referenced with the HyperLEDA database (Makarov et al. 2014). For SNe without listed host galaxies in TNS or in the literature, a query in the NED database of the local region was performed and the closest appropriate listed galaxy was considered to be the host galaxy. Following this, visual checks and comparison of the SNe and host redshifts were performed to ensure accuracy.

To fit elliptical isophotes to the host galaxies, we used archival images which are not contaminated by the SN. We obtained archival FITS (Wells, Greisen & Harten 1981) images of the host galaxies in visual bands (*V*, *g*, or equivalent) from the Pan-STARRS survey (Chambers et al. 2016), the DESI Legacy Sky Survey (Dey et al. 2019), the Sloan Digital Sky Survey (SDSS; Ahumada et al. 2020), or the Digitized Sky Surveys[3] (DSS). In these images, ellipses

were fit to the galaxies at constant levels of brightness using the `photutils.isophote` library (Bradley et al. 2020). This returns a list of isophote objects with attributes of semimajor axis (SMA), ellipticity, angle of rotation, the mean intensity value along the elliptical path (hereafter intensity), and the sum of all pixels inside the ellipse. The algorithm also provides a *k*-sigma clipping option for cleaning deviant sample points at each isophote. This improves the convergence stability against any nonelliptical structure such as stars, spiral arms, H II regions, and defects. The fit method is especially sensitive to initial conditions, and for those galaxies in which a fit could not converge or converged on visually clearly incorrect isophotes, the galaxy centre and ellipse attributes were determined manually to ensure accurate measurements of the intensity and flux values with `photutils.aperture.EllipticalAperture`.

As the isophotes get larger, the surface brightness of the galaxies is expected to decrease to zero because of the relative scarcity of stars, and thus the total-flux curve of growth will plateau at a constant flux value. As an example, Fig. 3 displays a curve of growth as a function of the SMA for the host galaxy of SN 2018evt, MCG -01-35-011. The inset in the figure shows an example of the fitted isophote containing SN 2018evt. For the Pan-STARRS and DESI Legacy images, the background noise in the images was negligible compared to the brightness of the galaxies, so the flux curve of growth did approach an apparent plateau. However, for the DSS images, the background level was measured by calculating the average of a manually selected area, and subtracted to ensure convergence, as the background was relatively high.

The size of the SMA at the SN location can be interpolated from the pair of closest isophotes between which the SN is enclosed using the SN's coordinates. This allows us to determine the fraction of the total flux contained within the isophote containing the SN, relative to the total flux of the galaxy. This value is the flux percentile, which is the normalized metric for the SN position in the host galaxy. For

[3]http://archive.eso.org/dss/dss/

Table 3. Polarization of 35 archival SNe from Cikota et al. (2019) in the *B* and *V* bands.

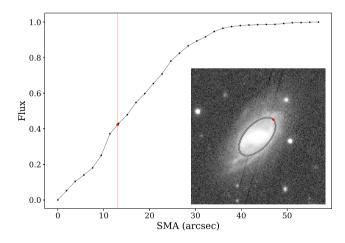| Name	MJD	Epoch	q_B (PER CENT)	u_B (PER CENT)	θ_B (°)	p_B (PER CENT)	q_V (PER CENT)	u_V (PER CENT)	θ_V (°)	p_V (PER CENT)
					SNe Ia in spiral host galaxies					
SN 2001dm	52134.33168	6.3	-0.23 ± 0.42	-0.21 ± 0.46	111.5 ± 39.9	0.0 ± 0.44	-0.04 ± 0.18	-0.35 ± 0.22	131.8 ± 39.9	0.21 ± 0.22
SN 2001el	52222.1011	39.6	-0.03 ± 0.09	0.61 ± 0.09	46.2 ± 4.0	0.6 ± 0.09	0.02 ± 0.04	0.62 ± 0.03	43.9 ± 4.0	0.62 ± 0.03
SN 2001V	51990.12065	17.5	0.14 ± 0.12	0.03 ± 0.24	5.1 ± 24.3	0.04 ± 0.12	0.14 ± 0.06	0.07 ± 0.05	12.3 ± 24.3	0.14 ± 0.06
SN 2002bo	52369.05487	12.6	-0.88 ± 0.1	-0.36 ± 0.11	101.2 ± 3.1	0.94 ± 0.1	-0.51 ± 0.08	-0.09 ± 0.05	95.0 ± 3.1	0.51 ± 0.08
SN 2002fk	52561.34352	13.4	0.28 ± 0.05	-0.23 ± 0.04	160.3 ± 3.6	0.36 ± 0.05	0.3 ± 0.04	-0.24 ± 0.04	160.5 ± 3.6	0.38 ± 0.04
SN 2003eh	52782.01566	0.0	1.22 ± 0.49	1.19 ± 0.42	22.1 ± 7.6	1.58 ± 0.45	0.65 ± 0.28	0.98 ± 0.35	28.3 ± 7.6	1.08 ± 0.33
SN 2003W	52673.26544	-6.7	-0.37 ± 0.14	-0.35 ± 0.25	111.7 ± 11.2	0.43 ± 0.2	-0.48 ± 0.17	-0.31 ± 0.12	106.6 ± 11.2	0.53 ± 0.15
SN 2004dt	53250.29035	10.3	0.17 ± 0.1	-0.28 ± 0.12	150.1 ± 9.9	0.29 ± 0.11	0.03 ± 0.1	-0.13 ± 0.08	142.3 ± 9.9	0.09 ± 0.08
SN 2004ef	53259.147	-5.3	0.04 ± 0.18	-0.37 ± 0.28	137.9 ± 21.3	0.17 ± 0.28	0.01 ± 0.3	-0.14 ± 0.27	136.1 ± 21.3	0.0 ± 0.27
SN 2004eo	53268.10228	-10.3	-0.08 ± 0.14	0.15 ± 0.1	59.1 ± 18.7	0.1 ± 0.11	-0.04 ± 0.17	0.09 ± 0.15	57.5 ± 18.7	0.0 ± 0.15
SN 2005de	53594.00508	-4.9	0.37 ± 0.09	0.02 ± 0.07	1.2 ± 6.8	0.35 ± 0.09	0.39 ± 0.1	0.03 ± 0.08	2.2 ± 6.8	0.37 ± 0.1
SN 2005df	53641.30388	42.1	-0.03 ± 0.05	-0.03 ± 0.06	113.0 ± 39.0	0.0 ± 0.06	0.06 ± 0.04	0.01 ± 0.03	7.0 ± 39.0	0.04 ± 0.04
SN 2005hk	53697.07734	11.7	-0.02 ± 0.12	-0.31 ± 0.16	133.6 ± 14.8	0.23 ± 0.16	0.08 ± 0.1	-0.23 ± 0.07	144.2 ± 14.8	0.23 ± 0.07
SN 2005ke	53691.08175	-8.1	0.16 ± 0.12	-0.13 ± 0.09	160.4 ± 15.4	0.15 ± 0.11	0.01 ± 0.11	-0.18 ± 0.06	137.0 ± 15.4	0.16 ± 0.06
SN 2006X	53825.15811	38.9	1.09 ± 0.28	-7.17 ± 0.29	139.3 ± 1.1	7.24 ± 0.29	0.96 ± 0.06	-6.03 ± 0.3	139.5 ± 1.1	6.09 ± 0.3
SN 2007fb	54298.31065	9.9	-0.66 ± 0.04	-0.23 ± 0.05	99.8 ± 1.6	0.7 ± 0.04	-0.6 ± 0.05	-0.21 ± 0.04	99.6 ± 1.6	0.63 ± 0.05
SN 2007le	54440.03806	40.7	0.92 ± 0.13	-1.58 ± 0.1	150.1 ± 1.7	1.82 ± 0.11	0.85 ± 0.07	-1.39 ± 0.05	150.7 ± 1.7	1.63 ± 0.06
SN 2007sr	54511.2502	63.4	0.05 ± 0.05	-0.03 ± 0.05	165.7 ± 24.9	0.01 ± 0.05	0.04 ± 0.05	0.0 ± 0.04	0.8 ± 24.9	0.0 ± 0.05
SN 2010ev	55387.98468	2.9	-1.8 ± 0.1	0.67 ± 0.08	79.8 ± 1.4	1.91 ± 0.09	-1.52 ± 0.09	0.67 ± 0.06	78.1 ± 1.4	1.66 ± 0.09
SN 2010ko	55539.19402	-6.0	-0.08 ± 0.13	0.12 ± 0.05	62.7 ± 17.1	0.09 ± 0.09	0.02 ± 0.88	0.1 ± 0.08	38.5 ± 17.1	0.0 ± 0.21
SN 2011ae	55624.18558	4.0	0.25 ± 0.04	0.21 ± 0.03	19.6 ± 3.1	0.32 ± 0.04	0.19 ± 0.05	0.15 ± 0.04	19.3 ± 3.1	0.23 ± 0.05
SN 2012fr	56267.31106	23.1	0.23 ± 0.06	0.06 ± 0.05	7.5 ± 7.5	0.23 ± 0.06	0.16 ± 0.01	0.0 ± 0.02	0.1 ± 7.5	0.16 ± 0.01
SN 2015ak	57273.07036	4.9	-0.36 ± 0.12	-1.27 ± 0.08	127.1 ± 1.9	1.31 ± 0.09	-0.34 ± 0.08	-1.13 ± 0.05	126.7 ± 1.9	1.17 ± 0.06
					SNe Ia in elliptical host galaxies					
SN 2004br	53144.03228	-3.9	-0.07 ± 0.14	0.2 ± 0.1	53.9 ± 13.5	0.17 ± 0.1	-0.03 ± 0.16	0.17 ± 0.13	49.7 ± 13.5	0.07 ± 0.14
SN 2008fl	54736.11925	15.3	0.77 ± 0.24	0.53 ± 0.17	17.4 ± 6.6	0.89 ± 0.22	0.84 ± 0.08	0.65 ± 0.09	18.8 ± 6.6	1.05 ± 0.09
SN 2011iv	55925.05084	19.5	0.09 ± 0.06	-0.08 ± 0.05	159.2 ± 14.0	0.09 ± 0.06	0.08 ± 0.02	-0.04 ± 0.03	166.1 ± 14.0	0.09 ± 0.03
					SNe Ia in S0 host galaxies					
SN 2002el	52501.18898	-7.6	0.03 ± 0.13	0.23 ± 0.11	40.7 ± 14.1	0.17 ± 0.11	0.06 ± 0.15	0.16 ± 0.12	35.2 ± 14.1	0.09 ± 0.12
SN 2003hv	52897.30336	6.1	0.03 ± 0.03	0.03 ± 0.05	25.0 ± 29.2	0.0 ± 0.04	0.02 ± 0.05	0.08 ± 0.03	38.5 ± 29.2	0.07 ± 0.03
SN 2003hx	52911.34071	18.8	-1.63 ± 0.39	1.0 ± 0.47	74.3 ± 6.2	1.83 ± 0.41	-1.12 ± 0.14	0.8 ± 0.12	72.2 ± 6.2	1.36 ± 0.13
SN 2005cf	53528.16586	-5.8	-0.61 ± 0.07	0.64 ± 0.04	66.8 ± 1.9	0.88 ± 0.06	-0.7 ± 0.07	0.61 ± 0.04	69.4 ± 1.9	0.93 ± 0.06
SN 2005el	53644.34433	-2.7	0.35 ± 0.13	-0.14 ± 0.11	169.2 ± 10.1	0.33 ± 0.13	0.41 ± 0.12	-0.15 ± 0.15	169.7 ± 10.1	0.4 ± 0.13
SN 2007hj	54361.10904	19.9	-0.16 ± 0.16	-0.26 ± 0.17	118.9 ± 15.2	0.22 ± 0.16	-0.13 ± 0.09	-0.14 ± 0.07	114.0 ± 15.2	0.16 ± 0.08
SN 2008ff	54735.17383	31.0	0.59 ± 0.21	-0.14 ± 0.14	173.4 ± 10.1	0.53 ± 0.21	0.46 ± 0.08	-0.08 ± 0.09	175.1 ± 10.1	0.45 ± 0.08
SN 2008fp	54736.33355	5.4	0.98 ± 0.06	-1.99 ± 0.05	148.2 ± 0.7	2.22 ± 0.05	0.78 ± 0.04	-1.62 ± 0.07	147.9 ± 0.7	1.8 ± 0.06
					SNe Ia in dwarf host galaxies					
SN 2007if	54363.17052	20.1	0.0 ± 0.7	-0.8 ± 0.28	135.1 ± 9.9	0.7 ± 0.28	-0.12 ± 0.14	-0.57 ± 0.11	129.0 ± 9.9	0.57 ± 0.11

Figure 3. Normalized flux curve of growth for MCG -01-35-011 (the host galaxy of SN 2018evt) as a function of SMA. The interpolated SMA of the isophote containing SN 2018evt is indicated with the red line. The inset shows the host galaxy MCG -01-35-011 and the isophote containing SN 2018evt. The position of the SN is marked with the red dot.

example, a SN located at the 95th flux percentile is located at the edge of the galaxy, with 95 per cent of the total flux contained inside of the isophote at which the SN lies.

The advantage of parameterizing the SN locations in terms of total-flux fractions is that the total-flux fractions determined by fitting

isophotes do not depend on the galaxies' inclinations, in contrast to normalized galactocentric distances using half-light radii or de Vaucouleurs radii.

3.4 Host-galaxy morphological classification

For 26 host galaxies without a given morphological classification in the NED or HyperLEDA databases, we searched for additional references or tried to classify them visually (Buta 2013) using archival images from either Pan-STARRS or the DESI Legacy Survey, and from available spectra. We classified 20 initially unclassified host galaxies, shown in Fig. 4. In the case of the host galaxy of SN 2019rm, there were no archival images from Pan-STARRS, the DESI Legacy Survey, or SDSS available. We show therefore an acquisition image obtained with FORS2 which contains the SN.

The host galaxy of SN 2007if is likely a dwarf galaxy (Scalzo et al. 2010). It is very faint and shows H α and [O II] $\lambda 3727$ emission lines at a heliocentric redshift of 0.07416 ± 0.00082 in a spectrum obtained on 2009 August 24.5 with the Low Resolution Imaging Spectrometer (LRIS) at the *Keck-I* 10-m telescope on Maunakea (Scalzo et al. 2010).

In addition to the host of SN 2019bjz looking like an elliptical galaxy in an image acquired by the Pan-STARRS survey, an archival SDSS spectrum also shows that the host displays a typical spectrum of an elliptical galaxy with strong absorption lines.

The host of SN 2019rm looks irregularly shaped; however, because of the low resolution of the available images, we could not
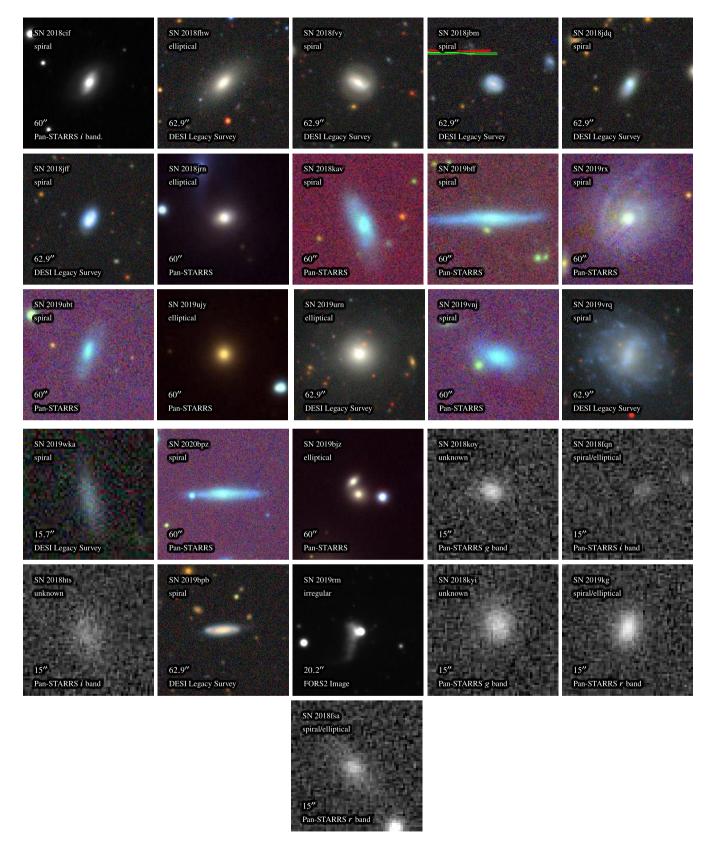
Figure 4. Host galaxies classified in this work. Indicated are the names of the SNe that occurred in the galaxies, our visual classifications, the image sources, and the widths of the images in arcseconds. Note that the image of the host galaxy of SN 2019rm is a FORS2 acquisition image (this work), so the SN is also visible, while the SNe are not visible in all other archival images from the Pan-STARRS Sky Survey and the DESI Legacy Sky Survey. The thumbnails are centred on the coordinates of the host galaxies.

successfully classify it. The hosts of SN 2018fsa, SN 2019bpb, and SN 2019kg display a bright core and a disc; however, the resolution of the available archival images is not sufficient to distinguish between spiral or elliptical galaxies. Furthermore, the hosts of SN 2018fqn, SN 2018hts, SN 2018koy, and SN 2018kyi are too faint and unresolved to be reliably classified.

The host galaxies of the SNe, their morphological classifications, the determined flux percentiles at the SN position, and image sources used to fit the isophotes are listed in Table 4. The galaxies for which the isophote fitting did not converge (i.e. if the isophotes were defined manually) have been flagged 'No' in the 'Fitted?' column.

4 RESULTS AND DISCUSSION

The goal of this work is to study the nature of dust, which is producing peculiar polarization and extinction properties along the sightlines to some SNe Ia. We investigated whether the steeply rising polarization curves toward blue wavelengths with relatively high degree of polarization, which are observed toward some SNe Ia, are produced by dust in the host-galaxy ISM or possible CSM associated with the progenitor system. If the dust in the ISM is responsible for producing the peculiar polarization curves, we would not expect to observe such polarization curves in elliptical galaxies, which are generally known to be dust poor. On the contrary, in spiral galaxies, which are dust rich, we may expect to observe an increased number of SNe with high polarization and steeply rising polarization curves closer to the galaxy centre compared to SNe in the outer parts of the spiral galaxies, because the dust abundance in spiral galaxies increases toward the galaxy centre (see e.g. Muñoz-Mateos et al. 2009; Cikota et al. 2016; Casasola et al. 2017).

We grouped our sample of SNe Ia according to the morphological classification of the host galaxies: (i) 66 SNe that occurred in spiral galaxies, (ii) 13 in elliptical galaxies, (iii) 15 in S0 galaxies, and (iv) 7 that occurred in a galaxy with unknown morphological classification. Additionally, there is one SN that exploded in a dwarf galaxy (SN 2007if) and one that exploded in an irregular galaxy (SN 2019rm). Thus, we observed a factor of five more SNe in spiral host galaxies than in elliptical galaxies. This is an expected frequency distribution over the morphological galaxy types (for comparison, see table 4 in van den Bergh, Li & Filippenko 2005).

We also analysed the polarization measurements of the SNe and distinguished between SNe that have polarization curves growing toward blue wavelengths (i.e. $p_B > p_V$), SNe with flat polarization curves (i.e. $p_B \approx p_V$), and SNe with Serkowski-like polarization curves (i.e. $p_B < p_V$). The polarization measurements for SNe in our sample that occurred before 2018 were taken from Cikota et al. (2019). For these 35 archival SNe, we have spectropolarimetric measurements over the range ~3800–9000 Å and the shape of the polarization curves can be visually inspected. SNe observed during 2018–2020 (this work) were observed in imaging-polarimetry mode in B, and eventually in V if the polarization in B was higher than 0.5 or 1 per cent (see Section 2.2). Therefore, the slope of the polarization curves is not known for the SNe with low polarization in B.

The sample is presented in Fig. 5 (SNe in spiral galaxies) and in Fig. 6 (all other SNe). The figures show the degree of polarization measured in the B band as a function of the fraction of flux within the isophote containing the SN relative to the total flux of the galaxy. Thus, the flux fraction represents the projected normalized location of the SN in the galaxy. It is known that the scale height of SNe Ia can be relatively high (e.g. Wang, Höflich & Wheeler 1997b), meaning that SNe Ia in spiral galaxies also explode far away from the galaxy plane. Therefore, depending on the scale height, the projected distance from

the centre may be different from the real distance. In other words, SNe Ia can appear to be projected very close to the galaxy centre, but in reality be very far from it. Furthermore, they can be located at the near or the far side of the galaxy, i.e. the line of sight may or may not pass through the galaxy. The black dots represent SNe with only one measurement in B; thus, there is no information on the shape of the polarization curve. Most of these SNe have low polarization and are not relevant for our study, and hence have not been observed in the V band as part of our survey (see Section 2.2).

4.1 SNe Ia in spiral versus elliptical galaxies

Most relevant to consider for our study is the difference between the degree of polarization of SNe in spiral versus elliptical galaxies. Fig. 5 shows SNe Ia that exploded in spiral host galaxies. 16 out of 66 SNe had polarization higher than 0.5 per cent in B, and 10 of them have polarization curves rising toward blue wavelengths. Particularly noticeable is that all SNe with very high polarization ($p_B \gtrsim 1$ per cent) have polarization curves rising toward blue wavelengths.

The figure also reveals that the polarization tends to be higher closer to the galaxy centre (at low flux percentiles). To demonstrate the trend of polarization as galactocentric distance decreases, we fit a linear function to SNe with polarization $p_B \gtrsim 0.5$ per cent (red line). The same trend is also visible if we only include SNe with polarization curves rising toward blue wavelengths (blue line), and if we exclude SN 2006X (grey dot–dashed line). Furthermore, the green bars represent the average polarization value of all SNe within 20 percentile wide bins. SNe located at the edges of their host galaxies (at distances above the 80th percentile) display low polarization, and SNe located close to the centre tend to have higher polarization. Because the polarization is higher close to the galactic centre, where there is more dust, the polarization is likely produced by the ISM. We note that the average polarization of all SNe within the first bin (closest to the galactic center, 0–20 percentile) is smaller than in the second bin (20–40 percentile). This may be due to a selection bias. Highly extincted SNe close to the galactic center are harder to discover than SNe with low dust-extinction levels. Inspection of the acquisition images of SN 2015ak, which may appear as an outlier with high polarization located far from the centre of its host galaxy, shows that it is actually located in the spiral arm (which are generally dust rich) of a strongly barred galaxy.

Fig. 6 (top panel) shows the B-band polarization for 15 SNe in elliptical, dwarf, and irregular galaxies. 13 SNe occurred in elliptical galaxies, and they all have low polarization values, except SN 2008fl, and SN 2007if which are outliers.

SN 2008fl was observed with FORS in spectropolarimetry mode, and displays a very flat (wavelength-independent) polarization curve with $p_B = 0.89 \pm 0.22$ per cent and $p_V = 1.05 \pm 0.09$ per cent. Furthermore, despite the absence of available imaging-polarization data preventing us from estimating the Galactic ISP using field stars, the MW reddening at the position of SN 2008fl is $E(B - V) = 0.157 \pm 0.006$ mag (Schlafly & Finkbeiner 2011). This implies a maximum polarization in the optical of ~1.4 per cent (Serkowski et al. 1975). An inspection of the flux spectra of SN 2008fl (Cikota et al. 2019) in the observer's frame also reveals the presence of interstellar Na I D lines in the MW. No such absorption features are visible in the host galaxy's rest frame. Therefore, the flat polarization curve in the case of SN 2008fl is likely produced by MW ISM.

SN 2007if, which is also shown in Fig. 6 and has a relatively high polarization in the B band, is an overluminous SN Ia ($M_V \approx -20.4$ mag) that exploded in a very faint dwarf host galaxy (Scalzo et al. 2010). SN 2007if has been observed at four epochs

Table 4. Host-galaxy information for the SN sample and the normalized SN positions in terms of flux percentile.

SNe name	Host	Morph.	Morph. source	Flux percentile	Image source	Fitted?
SN 2001dm	NGC 749	S	NED	0.286	Legacy Survey	Yes
SN 2001el	NGC 1448	Scd	NED	0.829	Legacy Survey	No
SN 2001V	NGC 3987	Sb	NED	0.931	Legacy Survey	No
SN 2002bo	NGC 3190	Sa	NED	0.464	Legacy Survey	Yes
SN 2002el	NGC 6986	S0$^-$	NED	0.955	Pan-STARRS	Yes
SN 2002fk	NGC 1309	Sbc	NED	0.264	Legacy Survey	Yes
SN 2003eh	MCG +01-29-3	Sb	NED	0.476	Legacy Survey	Yes
SN 2003hv	NGC 1201	S0°	NED	0.895	Legacy Survey	Yes
SN 2003hx	NGC 2076	S0$^+$	NED	0.070	DSS	Yes
SN 2003W	UGC 5234	Sc	NED	0.070	Legacy Survey	No
SN 2004br	NGC 4493	E	NED	0.269	Legacy Survey	Yes
SN 2004dt	NGC 799	Sa	NED	0.298	Legacy Survey	Yes
SN 2004ef	UGC 12158	Sb	NED	0.284	Legacy Survey	Yes
SN 2004eo[a]	NGC 6928	Sab	NED	0.955	Legacy Survey	Yes
SN 2005cf	MCG -01-39-3	S0	NED	0.999	Pan-STARRS	Yes
SN 2005de	UGC 11097	S	NED	0.910	Legacy Survey	No
SN 2005df	NGC 1559	Scd	NED	0.904	Legacy Survey	Yes
SN 2005el	NGC 1819	S0	NED	0.995	DSS	No
SN 2005hk	UGC 272	Sd	NED	0.853	Legacy Survey	No
SN 2005ke	NGC 1371	Sa	NED	0.664	Legacy Survey	Yes
SN 2006X	NGC 4321	Sbc	NED	0.380	Legacy Survey	Yes
SN 2007fb	UGC 12859	Sbc	NED	0.343	Legacy Survey	No
SN 2007hj	NGC 7461	S0	NED	0.659	Legacy Survey	Yes
SN 2007it[b]	...	Dwarf	Scalzo et al. (2010)	0.500		Yes
SN 2007le	NGC 7721	Sc	NED	0.127	Legacy Survey	Yes
SN 2007sr	NGC 4038	Sm	NED	1.000	DSS	No
SN 2008ff	ESO 284- G 032	S0/a	NED	0.991	DSS	Yes
SN 2008fl	NGC 6805	E	NED	0.652	DSS	Yes
SN 2008fp[c]	ESO 428-G14	S0°	NED	0.671	Pan-STARRS	Yes
SN 2010ev	NGC 3244	Scd	NED	0.105	DSS	No
SN 2010ko	NGC 1954	Sbc	NED	1.000	DSS	Yes
SN 2011ae	MCG -03-30-19	Scd	NED	0.199	Pan-STARRS	Yes
SN 2011iv	NGC 1404	E	NED	0.343	Legacy Survey	Yes
SN 2012fr	NGC 1365	Sb	NED	0.345	Legacy Survey	Yes
SN 2015ak	ESO 108-21	S	NED	0.873	Legacy Survey	No
SN 2018cif	IC 1422	S	This work	0.952	Pan-STARRS	Yes
SN 2018evt	MCG -01-35-011	S0$^-$	NED	0.433	Pan-STARRS	Yes
SN 2018fhw	WISEA J041805.98-633651.7	E	This work	0.564	Legacy Survey	Yes
SN 2018fhx	WISEA J062438.18-234354.5	S0°	NED	0.409	Pan-STARRS	Yes
SN 2018fnq	ESO 284- G 026	S0$^-$	LEDA	0.664	Legacy Survey	No
SN 2018fqd	2MASX J20515213-3650127	S	LEDA	0.697	DSS	Yes
SN 2018fqn[d]	GALEXASC J223938.25-150510.0	...	...	0.279	Pan-STARRS	Yes
SN 2018fsa	WISEA J222536.90-130431.5	S or E	This work	0.865	Pan-STARRS	Yes
SN 2018fuk	ESO 016- G 011	S	NED	0.911	DSS	Yes
SN 2018fvi	AM 0156-672	S	NED	0.715	DSS	No
SN 2018fvy	WISEA J013216.87-330602.3	S	This work	0.899	Legacy Survey	Yes
SN 2018fzm[e]	WISEA J210319.95-513250.7	S	NED	0.332	Pan-STARRS	Yes
SN 2018gyr	WISEA J004947.23-613914.0	S0	LEDA	0.526	Legacy Survey	Yes
SN 2018hsa	NGC 7038	Sc	NED	0.996	Pan-STARRS	Yes
SN 2018hsy	CGCG 091-100	Sa	LEDA	0.106	Pan-STARRS	Yes
SN 2018hts[f]	SDSS J232432.96+170537.9	...	...	0.617	Legacy Survey	No
SN 2018htt	NGC 1209	E	NED	0.093	Pan-STARRS	Yes
SN 2018jbm	LCRS B014013.3-453958	S	This work	0.997	DSS	No
SN 2018jdq	WISEA J112525.69-082759.8	S	This work	0.390	Pan-STARRS	Yes
SN 2018jeo	ESO 564- G 014	S	NED	1.000	Pan-STARRS	Yes
SN 2018jff	LCRS B234528.8-451528	S	This work	0.112	Legacy Survey	Yes
SN 2018jgn	WISEA J000255.82-265450.6	E	NED	0.140	Pan-STARRS	Yes
SN 2018jky	NGC 1329	Sa	NED	1.000	Pan-STARRS	Yes
SN 2018jny	SDSS J092438.14+252352.7	S	LEDA	0.979	Pan-STARRS	Yes
SN 2018jrn	ESO 575-IG 016 NED01	E	This work	0.355	Pan-STARRS	Yes
SN 2018jtj	SDSS J124103.32+080417.4	Sc	LEDA	0.624	Pan-STARRS	Yes
SN 2018kav	WISEA J045054.61-175913.1	S	This work	0.189	Pan-STARRS	Yes
SN 2018koy[g]	...	...	...	0.971	DSS	Yes
SN 2018kyi	WISEA J070709.55+261930.2	...	...	0.202	Pan-STARRS	Yes
SN 2019axg	MCG -01-27-027	Sab	LEDA	0.756	Pan-STARRS	Yes
SN 2019bak	WISEA J101331.71+293304.9	S	LEDA	0.041	Pan-STARRS	Yes
SN 2019baq	WISEA J122201.57+202030.1	E	LEDA	0.657	Pan-STARRS	Yes
SN 2019bdz	CGCG 048-018	Sbc	LEDA	0.901	Pan-STARRS	Yes
SN 2019bff	WISEA J141432.08+171358.6	S	This work	0.181	Pan-STARRS	No
SN 2019bjw	WISEA J105547.49+274016.3	Sb	LEDA	0.036	Pan-STARRS	Yes
SN 2019bjz[h]	III Zw 075 NOTES01	E	This work (SDSS Spectrum)	0.007	Pan-STARRS	Yes
SN 2019bkh	MCG +05-31-141	Sb	LEDA	0.125	Pan-STARRS	Yes
SN 2019bpb	WISEA J051209.21-435515.8	S or E	This work	0.996	DSS	Yes
SN 2019kg	WISEA J114245.72+214253.3	S or E	This work	0.016	Pan-STARRS	Yes

Table 4 *– continued*

SNe name	Host	Morph.	Morph. source	Flux percentile	Image source	Fitted?
SN 2019np	NGC 3254	Sbc	NED	0.853	Pan-STARRS	Yes
SN 2019rm	WISEA J055313.73-730655.3	Ir	This work (FORS2 Image)	0.780	DSS	No
SN 2019rx	WISEA J052200.10-071132.9	S	This work	0.643	Pan-STARRS	Yes
SN 2019rzm	MCG -03-04-038	S0a	LEDA	0.777	Pan-STARRS	Yes
SN 2019shq	ESO 432-IG 006 NED02	Sa	LEDA	0.241	DSS	Yes
SN 2019ubs	UGC 01895	Sc	NED	0.721	Pan-STARRS	Yes
SN 2019ubt	WISEA J232957.47+294943.5	S	This work	0.556	Pan-STARRS	Yes
SN 2019udk	CGCG 383-067	Sbc	LEDA	0.378	Pan-STARRS	Yes
SN 2019uhz	WISEA J014714.00-082745.2	Sab	LEDA	0.685	Legacy Survey	Yes
SN 2019ujy	2MASX J19415466-2010042	E	This work	0.135	Pan-STARRS	Yes
SN 2019ulp	UGC 04431	Sbc	NED	0.176	Legacy Survey	Yes
SN 2019umr	ESO 533- G 006	S	NED	0.204	Legacy Survey	Yes
SN 2019uoo	MCG -02-22-024	S0a	LEDA	0.523	Pan-STARRS	Yes
SN 2019upw	NGC 0109	Sa	NED	0.587	Legacy Survey	Yes
SN 2019urn	WISEA J005749.28-173826.7	E	This work	0.091	Legacy Survey	Yes
SN 2019vju	NGC 3514	Sc	NED	0.469	Pan-STARRS	Yes
SN 2019vnj	WISEA J110901.05-143809.5	S	This work	0.224	Pan-STARRS	Yes
SN 2019vrq	GALEXASC J030421.67-160124.7	S	This work	0.012	Legacy Survey	No
SN 2019vsa	IC 2995	Sc	NED	0.238	Pan-STARRS	No
SN 2019vv	CGCG 022-015	S0a	LEDA	0.581	Legacy Survey	No
SN 2019wka	SDSS J031440.16-005213.8	S	This work	0.375	Legacy Survey	No
SN 2019wqz	WISEA J114717.39-291104.3	S	LEDA	0.987	Pan-STARRS	Yes
SN 2020bpz	2MFGC 09157	S	This work	0.363	Pan-STARRS	No
SN 2020ckp	WISEA J083621.44-253200.8	Sbc	LEDA	0.283	Pan-STARRS	Yes
SN 2020clq	NGC 1613	S0$^+$	NED	0.307	Legacy Survey	Yes
SN 2020cpt	CGCG 076-111	E	LEDA	0.762	Legacy Survey	Yes
SN 2020ctr	WISEA J085837.55+201131.6	E	LEDA	0.016	Legacy Survey	Yes
SN 2020dvr	ESO 566- G 027	Sbc	NED	0.659	Pan-STARRS	Yes
SN 2020dyf	WISEA J153030.68-123612.4	Sb	NED	0.400	Pan-STARRS	Yes
SN 2020ejm	IC 2560	SB(r)b	NED	0.029	DSS	Yes

The morphological classifications are taken from NED (Helou et al. 1991), the HyperLEDA database (Makarov et al. 2014), or have been determined in this work. The 'Image source' indicates the source of the images used for the SN location determination, and the 'Fitted?' column indicates whether the isophote fitting converged.

^{a} Used red filter.
^{b} Host not listed in NED, the flux percentile was visually estimated.
^{c} Had to use z filter, gri filters had issues with artifacts.
^{d} Host data from the Sternberg Astronomical Institute Supernova Group.
^{e} Bright objects in proximity may affect the result.
^{f} Host data from Vizier.
^{g} Unknown host galaxy.
^{h} Too many objects in area, flux profile did not flatten.

between 13 and 46 d relative to peak brightness in spectropolarimetry mode (Cikota et al. 2019), and displays a time-independent and flat (wavelength-independent) continuum polarization of ∼0.7 per cent. Because there is no time dependence, the polarization is likely not intrinsic but produced by foreground dust. The Galactic reddening at the position of SN 2007if is $E(B - V) = 0.07 \pm 0.01$ mag (Schlafly & Finkbeiner 2011), which implies a maximum polarization in the optical of ∼0.6 per cent (Serkowski et al. 1975). The flux spectra of SN 2007if show significant interstellar lines from the MW, but no interstellar absorption lines from the host galaxy. Scalzo et al. (2010) derived $EW(Na I D) = 0.51^{+0.04}_{-0.05}$ Å for the Milky Way dust absorption, which corresponds to $E(B - V) = 0.072$ mag and is consistent with Schlafly & Finkbeiner (2011). Therefore, the polarization is likely produced only by MW dust.

Notably, none of the 13 SNe in elliptical galaxies have a polarization curve rising toward blue wavelengths. Although the sample of 13 SNe in elliptical galaxies is smaller compared to the sample of 66 SNe in spiral galaxies, ∼15 per cent of SNe in spiral galaxies have polarization curves rising toward blue wavelengths, which is ∼ 2 SNe out of 13. Assuming polarization curves rising toward the blue wavelengths is an intrinsic property of some SN Ia progenitor systems (e.g. the single-degenerate or core-degenerate systems), we would expect such polarization curves in 1–2 SNe that exploded in elliptical host galaxies. Despite the differences in the stellar populations between spiral and elliptical galaxies, all stellar populations between ∼0.1 and 10 Gyr are expected to produce

PPNe (Buzzoni, Arnaboldi & Corradi 2006; Miller Bertolami 2016). Therefore, the core-degenerate scenario is not a hallmark only of late-type galaxies.

4.2 Explanation of the peculiar dust properties

Our results indicate that in dust-rich spiral galaxies, high degree of polarization and polarization curves steeply rising toward blue wavelengths correlate with SNe in regions with denser ISM dust, as they are relatively closer to the centres of their host galaxies (see e.g. Muñoz-Mateos et al. 2009; Cikota et al. 2016; Casasola et al. 2017). We also observe that in elliptical galaxies, which are generally dust poor (Smith et al. 2012; Cikota et al. 2016), none of the SNe display polarization curves rising toward short wavelengths, and the polarization levels are low. Therefore, the steeply rising polarization curves observed toward some SNe Ia in spiral galaxies are likely related to host-galaxy ISM, and not to CSM originating from the progenitor system. However, note that the sample of 13 SNe in elliptical galaxies is small compared to the sample of 66 SNe in spiral galaxies (see Section 4.1). To unambiguously confirm the origin of the dust, the SN sample in elliptical galaxies should be increased in the future. A discovery of a SN Ia with a steeply rising polarization curve toward blue wavelengths in an elliptical galaxy would favour CSM for the origin of the peculiar dust.
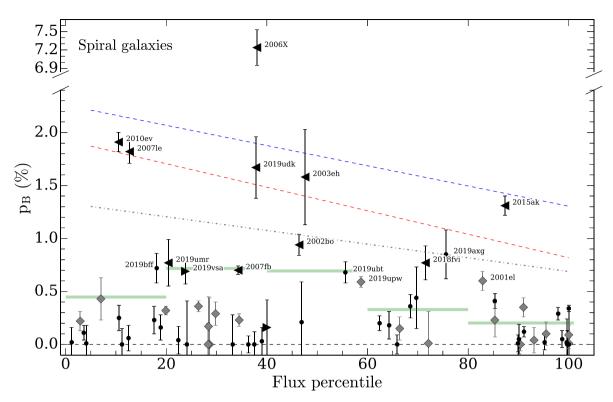
Figure 5. Polarization in the *B* band as a function of the host-galaxy flux percentile at the SN position. Shown here is the sample of SNe Ia that occurred in spiral galaxies. The flux percentile represents the normalized galactocentric distance of the SNe in their host galaxies. For example, a SN at a position of the 90th flux percentile is located near the edge of the galaxy, with 90 per cent of the total flux contained inside of the isophote at which the SN lies. The grey diamonds represent SNe with flat polarization curves, triangles pointing left are SNe with rising polarization curves toward blue wavelengths, and triangles pointing right mark SNe with polarization curves rising toward red wavelengths. The black dots represent SNe with only one measurement in the *B* band (so the slope of the polarization curves is not known). We fit a linear function to all SNe with polarization $p_B \gtrsim 0.5$ per cent (red line), and to SNe with polarization curves rising toward blue wavelengths and with polarization $p_B \gtrsim 0.5$ per cent (blue line). The grey dot–dashed line shows the same fit after excluding SN 2006X. The green bars represent the average polarization value of all SNe within bins of 20 percentile width.

However, constraining the origin of dust does not explain the peculiar dust properties. To produce the steeply rising polarization curves, a high abundance of small dust grains is required. The dust disruption process by the RAdiative Torque Disruption (RATD) mechanism may provide a possible explanation.

4.2.1 RATD mechanism induced by the SN radiation field

A possible explanation is that the strong radiation field of the SNe Ia, which explode in ISM-rich environments in their host galaxies, spin-up the nearby ($\lesssim 4$ pc) dust grains by radiative torques until they break apart owing to centrifugal forces, as suggested by Hoang et al. (2019). This RATD mechanism fragments large dust grains on relatively short time-scales, within days, depending on the dust distance from the SNe, and generates a high abundance of small dust grains, which can explain the low R_V values and the peculiar polarization curves with polarization maxima at short (blue) wavelengths (Hoang 2017; Hoang et al. 2019; Giang et al. 2020).

The probability that a SN event is going to happen close to an ISM dust cloud is higher at locations close to the centre of dust-rich galaxies (e.g. spiral galaxies), where the densities of dust are higher (as also suggested by Bulla et al. 2018b). This could explain why we observe that the SNe Ia with steeply rising polarization curves and higher polarization are located closer to the centre of their spiral host galaxies.

The RATD mechanism can be tested by polarimetry of highly polarized SNe at very early phases. Soon after the SN explosion, the dust around the SNe is gradually disrupted by the RATD mechanism as the SN brightens, and the polarization and the dust reddening are expected to be time-evolving before the destruction reaches maximum, as predicted by Giang et al. (2020). No such time evolution has ever been found so far (see e.g. fig. 4 of Zelaya et al. 2017), which can already set strong limits on the location of dust. It may imply that the dust distance is very near the SNe ($\ll 0.5$ pc) so that the dust disruption happens very soon after the explosion, before the SN is discovered or observed, or that the assumed parameters of the RATD and/or dust model need to be better constrained. However, theoretical modeling of dust destruction is beyond the scope of this paper. More spectropolarimetry of SNe starting within ~ 1 d after the explosion, especially of highly extinguished ones, will be most useful in the studies of polarization features related to dust destruction due to SN explosions.

Furthermore, the RATD is expected to work in all intense radiation fields, and therefore we expect to observe the effects of an increased abundance of small dust grains in the environments of other objects, such as core-collapse SNe, massive stars, active galactic nuclei (AGNs), gamma-ray bursts (GRBs), etc. (Hoang et al. 2019). Zafar et al. (2018) showed that typical extinction curves in GRB afterglows are consistent with the extinction curves observed in the Small Magellanic Cloud, and have a total-to-selective extinction ratio $R_V = 2.61 \pm 0.08$. Some core-collapse SNe, AGNs, and massive stars
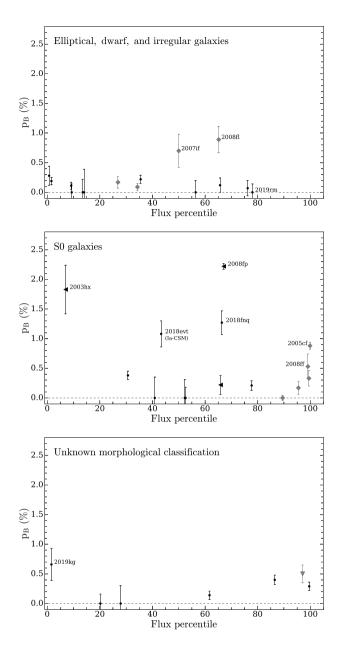
Figure 6. SN Ia polarization in *B* versus host-galaxy flux percentile at the SN position for different types of host galaxies. The flux percentile represents the location of the SN in the galaxy. The grey diamonds mark SNe with flat polarization curves, and the black dots are SNe with only one measurement (in the *B* band). *Top panel:* SNe in elliptical galaxies, SN 2019rm in a irregular galaxy, and SN 2007if in a dwarf galaxy. *Middle panel:* SNe in S0 galaxies. *Bottom panel:* The remaining SNe in morphologically unclassified galaxies.

also display polarization curves rising toward blue wavelengths (see e.g. Stevance et al. 2019, Hines et al. 2001, and Whittet et al. 1992, respectively). However, whether the extinction properties in these objects can be attributed to dust destruction from the RATD mechanism needs to be further investigated in a separate study.

4.2.2 RATD mechanism induced by the interstellar radiation field

Another possibility is that dust in the interstellar medium gets disrupted by the RATD mechanism owing to the interstellar radiation

field (Hoang 2021). Hoang (2021) suggest that extinction curves with R_V values in the range 1.5–2.5 can be produced by the interstellar radiation field (ISRF) if grains have composite structures of tensile strength $S_{\max} \lesssim 10^6$ erg cm^{-3}. The mean radiation intensity in main-sequence galaxies cannot produce high abundances of small dust grains that may explain the extremely low ($R_V \lesssim 1.5$) values observed toward some SNe Ia. However, such low R_V values may be explained if the mean intensity of these galaxies is enhanced by starbursts and the grain temperature can reach $T_d \approx 60$ K ($U \approx 10^3$, where $U = 1$ is the typical scale factor for the ISRF in the Solar neighbourhood). In that case, the extinction and polarization curves do not vary with time, in contrast to dust disruption induced by the SN radiation field (Giang et al. 2020). Although the typical mean starlight intensity scale factor U is low in galaxies in the local Universe ($U \lesssim 10$; Draine et al. 2007), U can range up to 10^7.

Some galaxies have significant fractions of dust luminosity radiated from regions with $U > 10^2$ (see tables 4 and 5 of Draine et al. 2007). The Spitzer Infrared Nearby Galaxy Survey (SINGS; Kennicutt et al. 2003) is an infrared imaging and spectroscopic survey of 75 nearby galaxies with a wide range of morphological types. Some of these SINGS galaxies have also been observed with the SCUBA camera (Holland et al. 1999) on the *James Clerk Maxwell Telescope* (*JCMT*), which made it possible to determine the ISRF (Draine et al. 2007). The median galaxy in the SINGS-SCUBA sample of 17 galaxies has 10 per cent of the dust luminosity originating in regions with $U > 10^2$ and ∼7.8 per cent in regions with $U > 10^3$ (see fig. 8 of Draine et al. 2007).

4.2.3 Possible differences between SN Ia populations

An alternative explanation that cannot be excluded is that the underlying progenitor populations of SNe Ia may be host-galaxy dependent. The lack of detected high continuum polarization in early-type galaxies may be a consequence of some systematic difference in the age or metallicity of the progenitors. Thus, some progenitor populations may imply different CSM environments and produce the peculiar extinction and polarization properties due to CSM scattering (see Section 1).

Wang et al. (2013) found that SNe Ia with high Si II velocity (HV SNe Ia) tend to explode at distances closer to the centre of the host galaxies than normal-velocity (NV) SNe Ia and are more likely to be associated with younger stellar environments and metal-rich progenitors. Furthermore, Wang et al. (2019) found that HV SNe Ia display a significant excess of blue flux 60–100 d past peak brightness compared to SNe with normal photospheric velocities. This excess may be attributed to light echoes by dust in the CSM.

Therefore, Wang et al. (2019) suggest that the HV SNe Ia may arise from single-degenerate progenitors. This is also consistent with the systematically observed blueshifted outflows in the Na I line (Sternberg et al. 2011; Maguire et al. 2013) in many SNe Ia. In contrast, SNe Ia that do not display HV features and possible evidence of CSM may have double-degenerate progenitor systems (Li et al. 2011; González Hernández et al. 2012; Schaefer & Pagnotta 2012; Olling et al. 2015; Wang et al. 2019).

The sub-M_{Ch} He-detonation (double-detonation) model may also explain the characteristics of HV and NV SNe Ia. In this scenario, the SN explosion becomes triggered by an initial detonation in the accreted He shell on the surface of the WD (e.g. Nomoto 1982a, b). Li et al. (2021) suggest that the observed diversity in the velocity arises from projection effects: HV SNe Ia are observed from the He-detonation side while NV SNe Ia are observed from the opposite side. On the other hand, Polin, Nugent & Kasen (2019) suggest that

different He-shell masses of exploding sub-M_{Ch} WDs may produce a range of Si II velocities. Pan (2020) found that HV SNe Ia tend to explode in massive environments with higher metallicities, while NV SNe Ia occur in both lower-mass and massive environments (see also Pan et al. 2015). This supports the possibility of multiple SN Ia populations and that HV SNe Ia may originate from exploding sub-Chandrasekhar-mass WDs because higher metallicities generally produce less-massive WDs (Pan 2020).

Studies of SN Ia rates in galaxies with different colour and morphological type (i.e. star-formation rates) implied that there may be two SN Ia populations: the promptly exploding and delayed SNe Ia (Scannapieco & Bildsten 2005; Mannucci, Della Valle & Panagia 2006; Sullivan et al. 2006). However, Maoz, Mannucci & Brandt (2012) found a continuous distribution of times between the formation of the progenitor systems and the SN explosions.

Besides different SN populations, an age dependency on SN Ia progenitors may also exist. Kang et al. (2020) claim to have found a significant correlation between the SN Ia luminosity and stellar population age. If true, SN Ia luminosity evolution can have a high impact on cosmology, because stellar populations get younger with increasing redshift. However, the result is highly debated and unlikely to be correct (Lee et al. 2020b, 2021; Rose et al. 2020; Murakami et al. 2021; Zhang et al. 2021).

4.3 Polarization angle alignment with galactic features

Zelaya et al. (2017) have shown that the polarization angles of reddened SNe Ia tend to be aligned with galactic features, notably the spiral arms of the host galaxies. Almost all SNe in their 'sodium-sample' that display sodium absorption lines in their spectra (and thus are clearly affected by dust) display polarization angles that are aligned with major features of their host galaxies, like the spiral arms or the disc. The most prominent example is SN 2006X, which displays almost perfect alignment of the polarization angle with the spiral arm (Fig. 7) in M100 (see also Patat et al. 2009, 2015). It is also in general known that the dust is aligned with the magnetic fields of the host galaxies; see e.g. Scarrott, Ward-Thompson & Warren-Smith (1987). These previous studies strongly suggest that the polarization is due to dust in the ISM.

The alignment of dust grains is also consistent with the RATD scenario. Although the RATD mechanism disrupts the dust grains, the disrupted and spinning grains quickly realign with the magnetic field. The spinning grains that contain unpaired electrons (e.g. silicates) tend to magnetize, which is known as the Barnett effect (Barnett 1915), and then start rapidly precessing about the external magnetic field, which establishes the axis of grain alignment (Dolginov & Mytrophanov 1976; Lee et al. 2020a).

We investigated the polarization angles of three SNe Ia observed in this work that exploded in spiral galaxies, have polarization curves rising toward blue wavelengths, and polarization higher than 0.5 per cent in the B band: SN 2018fvi, SN 2019umr, and SN 2019udk. As shown in Fig. 7, SN 2018fvi and SN 2019udk exhibit some level of coherence with the features of their hosts, but in the case of SN 2019udk it is difficult to determine as the SN is located on the major axis of the galaxy. SN 2019umr is not as well aligned as SN 2006X with its host galaxy's features, but as noted by Zelaya et al. (2017), lower polarization values introduce higher noise and systematic error (e.g. owing to the MW's ISP), and both SN 2018fvi and SN 2019umr are polarized <1 per cent compared to the polarization of nearly 2 per cent of SN 2019udk and over 7 per cent of SN 2006X. In general, it is also more difficult to determine the alignment with inclined, particularly edge-on galaxies, as features such as spiral arms are almost parallel to our line of sight in certain regions.

4.4 The cases of SN 2006X and SN 2014J

SN 2006X was a fast-expanding and highly reddened SN Ia that exploded in the nearby face-on spiral galaxy M100. Wang et al. (2008) determined the reddening $E(B - V)_{host} = 1.42 \pm 0.04$ mag with $R_V = 1.48 \pm 0.06$. SN 2006X also displayed a steeply rising polarization curve toward blue wavelengths with a polarization maximum at $\lambda_{max} \lesssim 0.4\,\mu m$ and a particularly high polarization in the B band, $p_B \approx 7.2$ per cent (Patat et al. 2009), compared to the rest of the sample which has $p_B \lesssim 2$ per cent.

Furthermore, Patat et al. (2007) detected temporal evolution in the blueshifted Na I D absorption lines in the spectra of SN 2006X, which implies that there is CSM dust around the SN, likely associated with the progenitor system. However, Patat et al. (2007) also derived an upper limit to the CSM shell that produced the variable Na I D lines at the relatively low mass of $3 \times 10^{-4}\,M_\odot$. This cannot explain the bulk of the reddening toward SN 2006X, as opposed to a deep, saturated, Na I D absorption line at a slightly different velocity, likely produced by a molecular cloud in the disc of the host galaxy M100 (see also Cox & Patat 2008). The evolution of the blueshifted Na I D lines has been explained by the authors with changes in the CSM ionization conditions induced by the variable SN radiation field.

The polarization angle is wavelength-independent (which implies that the dust grains of all sizes are well aligned), and aligned with the spiral arm. Therefore, as argued by Patat et al. (2009, 2015), it appears that the polarization along the sight line toward SN 2006X is produced by host-galaxy ISM with a high abundance of small dust grains. On the other hand, it is intriguing why the dust-size distribution in the host galaxy of SN 2006X, and other galaxies that display such peculiar polarization curves, would be so different compared to dust in the MW (Whittet et al. 1992; see also Cikota et al. 2018).

Hoang et al. (2019) offered an explanation by introducing the RATD mechanism (see Section 4.2), which we acknowledge as a possible explanation and which may also be valid for the case of SN 2006X and other SNe with similar polarization and dust-extinction properties. The prerequisite is that the molecular cloud along the sight line is not too distant from the SN.

SN 2014J occurred in the northern celestial hemisphere and is therefore not included in our VLT sample, but it is also a highly reddened and polarized SN Ia. The SN exploded in the nearly edge-on starburst galaxy M82, which was thought to be an irregular galaxy. However, Mayya, Carrasco & Luna (2005) found spiral arms and suggested a late morphological type SBc for M82. The SN exploded relatively close to the galactic center and displays an extinction of $E(B - V) = 1.37 \pm 0.03$ mag with $R_V = 1.4 \pm 0.1$ (Amanullah et al. 2014). The extinction can be explained by a combination of dust reddening and scattering (Foley et al. 2014; Welty et al. 2014; Yang et al. 2017, 2018).

Patat et al. (2014) obtained three spectropolarimetry epochs of SN 2014J (2014 January 28, February 3, and March 8), using the Calar Alto Faint Object Spectrograph (CAFOS) mounted at the 2.2-m telescope in Calar Alto, Spain (Patat & Taubenberger 2011). The SN exhibits an extremely steeply rising polarization curve with a polarization of 4.8 ± 0.6 per cent in the B band (Kawabata et al. 2014), 6.6 ± 0.1 per cent at 4000 Å, and a wavelength-independent polarization angle (Patat et al. 2015, see also Porter et al. 2016). The Na I D and K I features observed in a high-resolution spectrum reveal that the ISM toward SN 2014J is complex, with more than
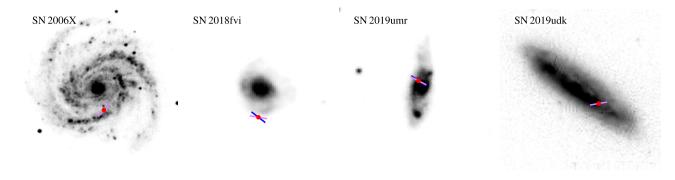
Figure 7. Polarization angles of (from left to right) SN 2006X, SN 2018fvi, SN 2019umr, and SN 2019udk. The blue and violet bars mark the polarization angles measured in the *B* and *V* bands, respectively. SN 2006X is an exemplary SN that displays an almost perfect alignment of the polarization angle with the spiral arm (Patat et al. 2009; Patat et al. 2015). SN 2018fvi shows some level of alignment with the host galaxy's features. The alignments of the polarization angles of SN 2019umr and SN 2019udk with possible spiral arms are debatable; it is difficult to determine the alignment in highly inclined galaxies.

five components placed at different distances (Patat et al. 2015). Therefore, Patat et al. (2015) suggest that the observed extinction and polarization properties reflect the average properties of the sight line, and exclude that the bulk of reddening and polarization is produced within one single cloud having peculiar properties. In this case, the rotational disruption by radiative torques (RATD) of dust along the sight line cannot be induced by the radiation field of the SN alone, but may be explained by RATD owing to the interstellar radiation field in this starburst galaxy (Hoang 2021; see also Section 4.2).

4.5 SNe Ia in lenticular galaxies and morphologically unclassified galaxies

Lenticular galaxies (S0) can have considerable amounts of dust; thus, it is not surprising that some of the SNe in our sample residing in those galaxies also exhibit high levels of polarization. 15 of our SNe that exploded in S0 galaxies, shown in the middle panel of Fig. 6. Six of them have polarization higher than 0.5 per cent in the *B* band, and two of these (SN 2003hx and SN 2008fp) have polarization curves rising toward blue wavelengths. SN 2003hx and SN 2008fp also show time-variable colour excess (Bulla et al. 2018b). Bulla et al. (2018b) inferred dust located at a distance of ~0.013 and ~9.4 pc from SN 2003hx and SN 2008fp, respectively.

SN 2018evt is a Type Ia-CSM SN, which exhibits strong emission of the Balmer lines most likely due to the interaction of the SN ejecta with CSM (e.g. Silverman et al. 2013). It displays a wavelength-independent continuum polarization of ~0.7 per cent at early epochs (Yang et al., in preparation). We have included SN 2018evt for completeness, because it was also observed as part of this program; however, because of its nature, it should be excluded from the analysis in this work.

SN 2018fnq displays a polarization of 1.3 ± 0.06 per cent in the *B* band, but only 0.21 ± 0.07 per cent in the *V* band. The *B* measurement may be systematically wrong; the peak values of the SN flux are only marginally below the saturation limit of the 16-bit A/D converter so that nonlinearities may have occurred.

Two objects (SN 2005cf and SN 2008ff) that display relatively high polarization are located near the edge of their host galaxies, where we do not expect significant amounts of ISM. SN 2005cf displays a normal Serkowski-like polarization curve with a peak of ~0.9 per cent (Cikota et al. 2019). The SN exploded at the edge of a tidal stream between two interacting galaxies, MCG -01-39-003 and NGC 5917. Pastorello et al. (2007) reported a negligible host-galaxy reddening and nondetection of host-galaxy interstellar absorption lines. The Galactic reddening toward the SN is $E(B - V)$

$= 0.084 \pm 0.001$ mag (Schlafly & Finkbeiner 2011), which might be just sufficient to explain the observed polarization (Serkowski et al. 1975). Wang et al. (2009a), however, report clearly visible interstellar Na I D lines from the host galaxy and the MW in the spectrum of SN 2005cf, and determine a reddening of $E(B - V)_{host} = 0.10 \pm 0.03$ mag, and thus a total reddening of $E(B - V) \approx 0.2$ mag. Therefore, despite the large distance from the host-galaxy centre, CSM can likely be excluded as the origin of the relatively high polarization, which can be explained as a combination of ISM in the tidal stream and MW reddening.

SN 2008ff displays a wavelength-independent polarization curve (Cikota et al. 2019) of $p = 0.5 \pm 0.2$ per cent. The MW reddening toward the SN is $E(B - V) = 0.044 \pm 0.001$ mag (Schlafly & Finkbeiner 2011). This amount of reddening may produce polarization up to ~0.4 per cent (Serkowski et al. 1975), and within the errors it may explain the observed polarization. Unfortunately, there are no detailed studies of SN 2008ff in the literature, so the host-galaxy extinction is not determined.

SN 2018koy, which exploded in a galaxy of unknown morphological classification, is located relatively far from the host galaxy's centre and has a significant polarization of >1 per cent. However, as shown in Fig. 2, the high polarization is associated with large interstellar polarization produced by MW dust.

5 SUMMARY AND CONCLUSIONS

The goal of this work is to study whether the peculiar polarization curves observed toward some SNe Ia are produced by ISM or CSM. In order to understand what may cause the non-standard dust properties toward SNe Ia, we conducted an imaging linear polarization survey of 69 SNe Ia with the VLT and FORS2 between 2018 and 2020. Additionally, we combined the sample with archival spectropolarimetric data for 35 SNe Ia observed with the FORS1/2 between 2001 and 2015. We investigated whether there is a relation between the continuum degree of polarization of SNe Ia and the galactocentric distances, for galaxies of different morphological classifications and host-galaxy dust properties. Our main results can be summarized as follows:

(i) 16 out of 66 SNe Ia that exploded in spiral host galaxies (Fig. 5) display significant polarization in the *B* band ($p_B > 0.5$ per cent), and 10 of these 16 exhibit polarization curves rising toward blue wavelengths. Furthermore, all six SNe with $p_B > 1$ per cent have polarization curves rising toward blue wavelengths. The polarization of SNe closer to the galactic centre tends to be

higher, while the SNe located at the edge of the galaxy (at locations $> 80^{th}$ flux percentile) have low continuum polarization, on average $p_B \approx 0.2$ per cent. On the contrary, 13 SNe Ia that exploded in elliptical host galaxies (shown in Fig. 6), which are generally dust-poor, all display low polarization, $p_B \lesssim 0.3$ per cent (except one outlier affected by MW ISP), and none of the SNe display polarization curves rising toward short wavelengths. Therefore, the steeply rising polarization curves observed toward some SNe Ia are likely related to dust in the host-galaxy ISM, as opposed to CSM originating from the progenitor system (see discussion in Section 4.1 and Section 4.2). This result is consistent with the conclusion by Patat et al. (2015) that the anomalous polarization curves are most probably produced by interstellar dust. Also, Kawabata et al. (2014) concluded that the observed polarization in the case of SN 2014J is likely predominantly caused by the interstellar dust. Furthermore, our result provides evidence that the effect of dust on SNe Ia can be different in spiral and elliptical galaxies, which could change the SN colours and brightness in different ways, and thus introduce some systematic bias in the luminosity standardization of these SNe.

(ii) All SNe Ia (except SN 2019vsa) with measured polarization above ~ 0.7 per cent in the *B* band and measured slopes have blueward-rising polarization curves. This implies that for strong polarization to occur toward SNe Ia the dust grains are almost always small.

(iii) Our original hope was that the observations would also reveal the reasons why dust toward SNe Ia seems to have peculiar properties. However, this conundrum is still not unambiguously resolved. We discuss several possible explanations.

(iv) The peculiar, steeply rising polarization curves toward blue wavelengths may be explained through destruction of nearby dust in the ISM by the RATD mechanism induced by the strong radiation field of the SNe, as suggested by Hoang et al. (2019). The RATD mechanism generates a high abundance of small dust grains, which can explain the low R_V values and the peculiar polarization curves observed toward some SNe Ia (Hoang 2017; Hoang et al. 2019; Giang et al. 2020). Because of the dust distribution within the host galaxies, the probability that a SN will explode close to a dust cloud is higher at locations near the centre of dust-rich galaxies such as spirals (Bulla et al. 2018b). This may explain why the steeply rising polarization curves of SNe Ia and the relation of the degree of polarization with galactocentric distance are observed for SNe that exploded in dust-rich spiral host galaxies, in contrast to the dust-poor elliptical galaxies. However, there is a caveat to this model: Giang et al. (2020) predicted that dust disruption by the RATD mechanism should produce temporal evolution of the continuum polarization, which has not been observed toward SNe Ia (see e.g. fig. 4 of Zelaya et al. 2017).

(v) Dust in the interstellar medium may also get disrupted by the RATD mechanism owing to the interstellar radiation field (Hoang 2021). A significant fraction of dust (~ 8 per cent) in the SINGS galaxies is located in regions with $U > 10^3$ (Draine et al. 2007). Such radiation intensity may generate a high abundance of small dust grains by the RATD mechanism to explain the low R_V values and polarization curves peaking at $\lambda_{max} < 0.4$ µm. In that case, time variability of SN Ia extinction and polarization measurements is not expected to be observed.

(vi) The polarization angle alignment with galactic features (see e.g. Zelaya et al. 2017) is also consistent with the assumed RATD mechanism, because the disrupted and spinning dust grains can realign in the magnetic field owing to the Barnett effect (Barnett 1915; Lee et al. 2020a).

(vii) An alternative explanation that because of some systematic differences in the age or metallicities between the progenitor populations in the early-type and late-type galaxies some progenitor populations may imply different CSM environments cannot be excluded.

DATA AVAILABILITY

The data underlying this article are available in the article. The raw data can be accessed online from the ESO Science Archive Facility.

REFERENCES

Ahumada R. et al., 2020, ApJS, 249, 3
Amanullah R. et al., 2014, ApJ, 788, L21
Amanullah R. et al., 2015, MNRAS, 453, 3300
Andersson B. G. et al., 2013, ApJ, 775, 84
Appenzeller I. et al., 1998, Messenger, 94, 1
Ashall C. et al., 2021, ApJ, 922, 205
Barnett S. J., 1915, Phys. Rev., 6, 239
Bellm E. C. et al., 2019, PASP, 131, 018002
Bertin E., Arnouts S., 1996, A&AS, 117, 393
Bradley L. et al., 2020, astropy/photutils: 1.0.0
Bulla M., Goobar A., Amanullah R., Feindt U., Ferretti R., 2018a, MNRAS, 473, 1918
Bulla M., Goobar A., Dhawan S., 2018b, MNRAS, 479, 3663
Burns C. R. et al., 2014, ApJ, 789, 32
Buta R. J., 2013, Galaxy Morphology. Springer Netherlands, Dordrecht, p. 1

Buzzoni A., Arnaboldi M., Corradi R. L. M., 2006, MNRAS, 368, 877
Casasola V. et al., 2017, A&A, 605, A18
Chambers K. C. et al., 2016, preprint (arXiv:1612.05560)
Chiotellis A., Boumis P., Spetsieri Z. T., 2021, MNRAS, 502, 176
Cikota A., Deustua S., Marleau F., 2016, ApJ, 819, 152
Cikota A., Patat F., Cikota S., Spyromilio J., Rau G., 2017, MNRAS, 471, 2111
Cikota A. et al., 2018, A&A, 615, A42
Cikota A. et al., 2019, MNRAS, 490, 578
Cox N. L. J., Patat F., 2008, A&A, 485, L9
Dey A. et al., 2019, AJ, 157, 168
Dolginov A. Z., Mytrophanov I. G., 1976, Ap&SS, 43, 257
Draine B. T., 2003, ARA&A, 41, 241
Draine B. T., Fraisse A. A., 2009, ApJ, 696, 1
Draine B. T. et al., 2007, ApJ, 663, 866
ESO, 2021, FORS2 User Manual
Folatelli G. et al., 2010, AJ, 139, 120
Foley R. J. et al., 2014, MNRAS, 443, 2887
Gaia Collaboration, 2016, A&A, 595, A1
Giang N. C., Hoang T., Tram L. N., 2020, ApJ, 888, 93
González Hernández J. I., Ruiz-Lapuente P., Tabernero H. M., Montes D., Canal R., Méndez J., Bedin L. R., 2012, Nature, 489, 533
González-Gaitán S., Mourão A. M., Patat F., Anderson J. P., Cikota A., Wiersema K., Higgins A. B., Silva K., 2020, A&A, 634, A70
Helou G., Madore B. F., Schmitz M., Bicay M. D., Wu X., Bennett J., 1991, The NASA/IPAC Extragalactic Database. Springer, Dordrecht, p. 89
Hines D. C., Schmidt G. D., Gordon K. D., Smith P. S., Wills B. J., Allen R. G., Sitko M. L., 2001, ApJ, 563, 512
Hoang T., 2017, ApJ, 836, 13
Hoang T., 2021, ApJ, 907, 37
Hoang T., Lazarian A., Martin P. G., 2013, ApJ, 779, 152
Hoang T., Lazarian A., Martin P. G., 2014, ApJ, 790, 6
Hoang T., Tram L. N., Lee H., Ahn S.-H., 2019, Nat. Astron., 3, 766
Holland W. S. et al., 1999, MNRAS, 303, 659
Hsiao E. Y. et al., 2020, ApJ, 900, 140
Ilkov M., Soker N., 2012, MNRAS, 419, 1695
Ilkov M., Soker N., 2013, MNRAS, 428, 579
Jedrzejewski R. I., 1987, MNRAS, 226, 747
Jones D., Boffin H. M. J., 2017, Nat. Astronomy, 1, 0117
Kang Y., Lee Y.-W., Kim Y.-L., Chung C., Ree C. H., 2020, ApJ, 889, 8
Kashi A., Soker N., 2011, MNRAS, 417, 1466
Kawabata K. S. et al., 2014, ApJ, 795, L4
Kennicutt Robert C. J. et al., 2003, PASP, 115, 928
Lee H., Hoang T., Le N., Cho J., 2020a, ApJ, 896, 44
Lee Y.-W., Chung C., Kang Y., Jee M. J., 2020b, ApJ, 903, 22

Lee Y.-W., Chung C., Demarque P., Park S., Son J., Kang Y., 2021, preprint (arXiv:2107.06288)
Li W. et al., 2011, Nature, 480, 348
Li W. et al., 2021, ApJ, 906, 99
Livio M., Mazzali P., 2018, Phys. Rep., 736, 1
Livio M., Riess A. G., 2003, ApJ, 594, L93
Maguire K. et al., 2013, MNRAS, 436, 222
Makarov D., Prugniel P., Terekhova N., Courtois H., Vauglin I., 2014, A&A, 570, A13
Mannucci F., Della Valle M., Panagia N., 2006, MNRAS, 370, 773
Maoz D., Mannucci F., Brandt T. D., 2012, MNRAS, 426, 3282
Maoz D., Mannucci F., Nelemans G., 2014, ARA&A, 52, 107
Mayya Y. D., Carrasco L., Luna A., 2005, ApJ, 628, L33
Miller Bertolami M. M., 2016, A&A, 588, A25
Muñoz-Mateos J. C. et al., 2009, ApJ, 701, 1965
Murakami Y. S., Stahl B. E., Zhang K. D., Chu M. R., McGinness E. C., Patra K. C., Filippenko A. V., 2021, MNRAS, 504, L34
Nobili S., Goobar A., 2008, A&A, 487, 19
Nomoto K., 1982a, ApJ, 253, 798
Nomoto K., 1982b, ApJ, 257, 780
Olling R. P. et al., 2015, Nature, 521, 332
Oppenheimer B. D., Bieging J. H., Schmidt G. D., Gordon K. D., Misselt K. A., Smith P. S., 2005, ApJ, 624, 957
Pan Y. C., Sullivan M., Maguire K., Gal-Yam A., Hook I. M., Howell D. A., Nugent P. E., Mazzali P. A., 2015, MNRAS, 446, 354
Pan Y.-C., 2020, ApJ, 895, L5
Pastorello A. et al., 2007, MNRAS, 376, 1301
Patat F., Romaniello M., 2006, PASP, 118, 146
Patat F., Taubenberger S., 2011, A&A, 529, A57
Patat F. et al., 2007, Science, 317, 924
Patat F., Baade D., Höflich P., Maund J. R., Wang L., Wheeler J. C., 2009, A&A, 508, 229
Patat F. et al., 2014, Astron. Telegram, 5830, 1
Patat F. et al., 2015, A&A, 577, 53
Perlmutter S. et al., 1999, ApJ, 517, 565
Phillips M. M. et al., 2013, ApJ, 779, 38
Polin A., Nugent P., Kasen D., 2019, ApJ, 873, 84
Porter A. L. et al., 2016, ApJ, 828, 24
Riess A. G. et al., 1998, AJ, 116, 1009
Rose B. M. et al., 2020, ApJ, 896, L4
Scalzo R. A. et al., 2010, ApJ, 713, 1073
Scannapieco E., Bildsten L., 2005, ApJ, 629, L85
Scarrott S. M., Ward-Thompson D., Warren-Smith R. F., 1987, MNRAS, 224, 299
Schaefer B. E., Pagnotta A., 2012, Nature, 481, 164
Schlafly E. F. et al., 2016, ApJ, 821, 78
Schlafly E. F., Finkbeiner D. P., 2011, ApJ, 737, 103
Serkowski K., Mathewson D. S., Ford V. L., 1975, ApJ, 196, 261
Silverman J. M. et al., 2013, ApJS, 207, 3
Smartt S. J. et al., 2015, A&A, 579, A40
Smith M. W. L. et al., 2012, ApJ, 748, 123
Soker N., 2019a, New A Rev., 87, 101535
Soker N., 2019b, MNRAS, 490, 2430
Sternberg A. et al., 2011, Science, 333, 856
Stetson P. B., 1987, PASP, 99, 191
Stevance H. F. et al., 2019, MNRAS, 485, 102
Sullivan M. et al., 2006, ApJ, 648, 868
Tody D., 1986, in Crawford D. L., ed., Proc. SPIE Conf. Ser, Vol. 627, Instrumentation in Astronomy VI. SPIE, Bellingham. p. 733
Urbaneja M. A., Kudritzki R. P., Gieren W., Pietrzyński G., Bresolin F., Przybilla N., 2017, AJ, 154, 102
van den Bergh S., Li W., Filippenko A. V., 2005, PASP, 117, 773
van Dokkum P. G., 2001, PASP, 113, 1420
Wang L., Wheeler J. C., 2008, ARA&A, 46, 433
Wang L., Wheeler J. C., Höflich P., 1997a, ApJ, 476, L27
Wang L., Höflich P., Wheeler J. C., 1997b, ApJ, 483, L29
Wang X. et al., 2008, ApJ, 675, 626
Wang X. et al., 2009a, ApJ, 697, 380

Wang X. et al., 2009b, ApJ, 699, L139

Wang X., Wang L., Filippenko A. V., Zhang T., Zhao X., 2013, Science, 340, 170

Wang X., Chen J., Wang L., Hu M., Xi G., Yang Y., Zhao X., Li W., 2019, ApJ, 882, 120

Wells D. C., Greisen E. W., Harten R. H., 1981, A&AS, 44, 363

Welty D. E., Ritchey A. M., Dahlstrom J. A., York D. G., 2014, ApJ, 792, 106

Whittet D. C. B., van Breda I. G., 1978, A&A, 66, 57

Whittet D. C. B., Martin P. G., Hough J. H., Rouse M. F., Bailey J. A., Axon D. J., 1992, ApJ, 386, 562

Wu C., Liu D., Wang X., Wang B., 2021, MNRAS, 503, 4061

Yang Y. et al., 2017, ApJ, 834, 60

Yang Y. et al., 2018, ApJ, 854, 55

Zafar T. et al., 2018, MNRAS, 479, 1542

Zelaya P. et al., 2017, ApJ, 836, 19

Zhang K. D., Murakami Y. S., Stahl B. E., Patra K. C., Filippenko A. V., 2021, MNRAS, 503, L33

This paper has been typeset from a TEX/LATEX file prepared by the author.